

Article

Thermomechanical Optimization of Three-Dimensional Low Heat Generation Microelectronic Packaging Using the Boundary Element Method

José Vallepuja-Espinosa , Jaime Cifuentes-Rodríguez , Víctor Gutiérrez-Posada and Iván Ubero-Martínez * 

Departamento de Tecnología Minera, Topográfica y de Estructuras, Universidad de León, Campus de Vegazana, s/n, 24071 León, Spain; jvale@unileon.es (J.V.-E.); jcifr@unileon.es (J.C.-R.); gutierrezposada.v@gmail.com (V.G.-P.)

* Correspondence: iubem@unileon.es

Abstract: This paper presents a simulation based on the boundary element method for the optimization of the thermomechanical behavior of three-dimensional microchip-dissipator packaging when the heat generation produced is medium-low. Starting from a basic architecture studied in the literature, different modifications affecting both elastic boundary conditions and the contact interface between the microprocessor and the heatsink are included and studied in order to improve heat dissipation. A nonlinear interface material is included at the interface of both solids. Thus, a thermal contact conductance as a function of the normal contact traction is simulated. Finally, all these improvements in both contact interface and boundary conditions are applied to study the maximum heat generation that this kind of architecture can efficiently dissipate, so that the microchip will not be damaged due to thermal deformations.

Keywords: boundary element method; elastic contact problem; thermoelastic contact problem; microelectronic packaging; variable thermal contact resistance; thermal interface material

MSC: 65N38; 74S15; 80M15



Citation: Vallepuja-Espinosa, J.; Cifuentes-Rodríguez, J.; Gutiérrez-Posada, V.; Ubero-Martínez, I. Thermomechanical Optimization of Three-Dimensional Low Heat Generation Microelectronic Packaging Using the Boundary Element Method. *Mathematics* **2022**, *10*, 1913. <https://doi.org/10.3390/math10111913>

Academic Editor: James M. Buick

Received: 22 April 2022

Accepted: 28 May 2022

Published: 2 June 2022

Publisher's Note: MDPI stays neutral with regard to jurisdictional claims in published maps and institutional affiliations.



Copyright: © 2022 by the authors. Licensee MDPI, Basel, Switzerland. This article is an open access article distributed under the terms and conditions of the Creative Commons Attribution (CC BY) license (<https://creativecommons.org/licenses/by/4.0/>).

1. Introduction

When the heat generation in the CPU microelectronic packaging is low (<20 W), the most commonly used packaging architecture is the one shown in Figure 1 where the heatsink simply rests on the microprocessor. This situation was modeled in [1], in which the behavior of the complete heatsink–microprocessor assembly was simulated, obtaining the normal traction distribution in the contact zone and the maximum temperatures on the microprocessor. Ref. [1] concluded that above certain constant clamping pressure in the top face of the heatsink, due to the fact that the heatsink is larger than the microprocessor, very high normal contact tractions appeared at the edges of the microprocessor due to a cantilever effect. In addition, this effect is accompanied by a decrease of the normal tractions at the center which could lead to detachments at this area. Moreover, the increment of heat coming from the CPU increased these effects due to the higher thermal deformations. Thus, the microelectronic packaging architecture shown in Figure 1 was limited to low heat generation.

In order to reduce this double effect and to increase the cooling capacity of the microelectronic packaging, in this work are studied different modifications to the architecture shown in Figure 1. Firstly, the heatsink is going to be supported on its edges in order to minimize the cantilever effect. This modification is going to constrain even more the deformations of the heatsink and the supports are going to support part of the applied clamping pressure on the heatsink, leading to a more uniform normal traction distribution at the contact zone between the heatsink and the microprocessor. Secondly, instead of applying a constant clamping pressure on the upper face of the heatsink, a retention mechanism is

simulated by means of Winkler elastic supports [2]. Thus, the clamping pressure is going to depend on the deformation of the face as a function of the elastic supports stiffness (K).

This improvement leads to a better normal traction distribution at the contact zone between both solids.

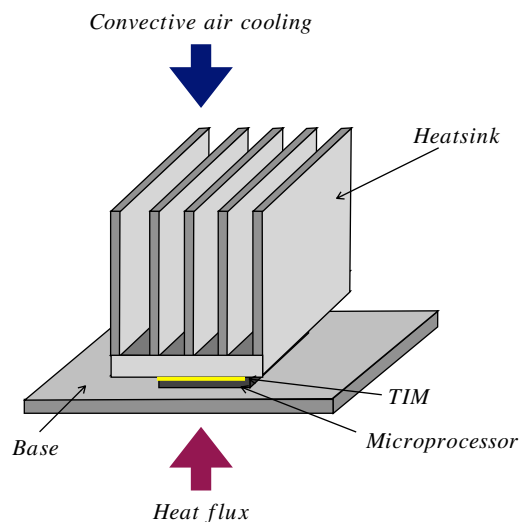


Figure 1. Typical low heat generation microelectronic packaging architecture.

Moreover, it is well known that in thermomechanical contact, the resulting interface between both solids in contact consists of numerous microcontacts and microgaps. Thus, a thermal contact resistance [3–5] is created since the heat flow has to go through these microgaps from one surface to the other. This thermal contact resistance increases the nonlinearity inherent in the problem as the temperature values along the contact zone becomes dependent on the traction values. In [1], vacuum conditions were assumed at the interface between both solids, so the heat flow transmission was very inefficient since it occurred only through the microcontacts. Moreover, the contact zone was very dependent on the normal contact traction which is limited by the microprocessor mechanical strength. For this reason, this work also includes a thermal interface material (TIM) fulfilling the microgaps in order to increase the thermal contact conductance as it has been demonstrated in [4,6].

There are several works focused on the study of the thermal impedance [7,8], the cooling performance [9,10] and different thermal resistances models [11,12] on microelectronic packaging. To the best of the authors' knowledge, only [1] has analyzed the thermoelastic contact in microelectronic packaging and so, this work is the first one in which enhancements of three-dimensional low heat generation microelectronic packaging are studied in order to improve its cooling capacity.

The thermomechanical contact has been studied using different numerical formulations. Based on the Finite Element Method (FEM), works have been published [13–21] concerning different kinds of thermomechanical contact problem involving friction and/or wear. On the other hand, it is well known that the Boundary Element Method (BEM) is very suitable for solving mechanical interface interaction problems [22]. Thus, the BEM has been applied to study the thermomechanical contact problem in 2D [23,24] and in 3D [6,25–29] and the elastic contact including friction and wear in [30–33].

In this context, this work is focused in the study of improvements to get a better cooling capacity of low heat generation microelectronic packaging. For this reason, different modifications in both elastic boundary conditions and at the contact zone are studied. As it was stated above, in order to save the nonlinearity inherent in the problem, the BEM has been used in order to get thermomechanical variables in low heat generation microelectronic packaging.

This paper is structured as follows: Section 2 presents the governing equations of the problem. The nonlinear thermomechanical contact conditions are presented in Section 3. The boundary element thermomechanical discrete equations have been described in Section 4. Section 5 is focused in the simulation of the improvements performed in the low heat generation microelectronic packaging in order to obtain a better cooling capacity. Moreover, once these improvements have been simulated, the heat generated in the microchip will be progressively increased in order to approximately determinate when the architecture herein presented stops being efficient in heat dissipation and it is necessary to find other type of solutions. Finally, the paper is finished with the summary and the concluding remarks.

2. Governing Equations and Boundary Conditions

The contact problem between two 3D thermoelastic isotropic bodies $\Omega^l \subset \mathbb{R}^3$ ($l = A, B$) under quasistatic thermoelastic contact conditions with a piecewise smooth boundary Γ^l , in a Cartesian coordinate system (xyz) (see Figure 2). The mechanical and thermal boundary conditions are defined using two partitions of Γ^l . The thermal partition is divided into four disjoint parts: Γ_{θ}^l , on which the temperature $\bar{\theta}$ is imposed, Γ_q^l with heat flux \bar{q} prescribed, Γ_{FC}^l on which forced convection conditions $\bar{\theta}_f, \bar{h}_f$ are imposed and Γ_c^l , which is defined as the potential contact zone. The mechanical partition is: $\Gamma^l = \Gamma_t^l \cup \Gamma_u^l \cup \Gamma_K^l \cup \Gamma_c^l$, being the traction \bar{t}_i assumed on Γ_t^l , the elastic displacements \bar{u}_i prescribed on Γ_u^l , elastic retention mechanism modeled by means of Winkler elastic supports prescribed on Γ_K^l with K known and Γ_c^l , which is defined as the potential contact zone.

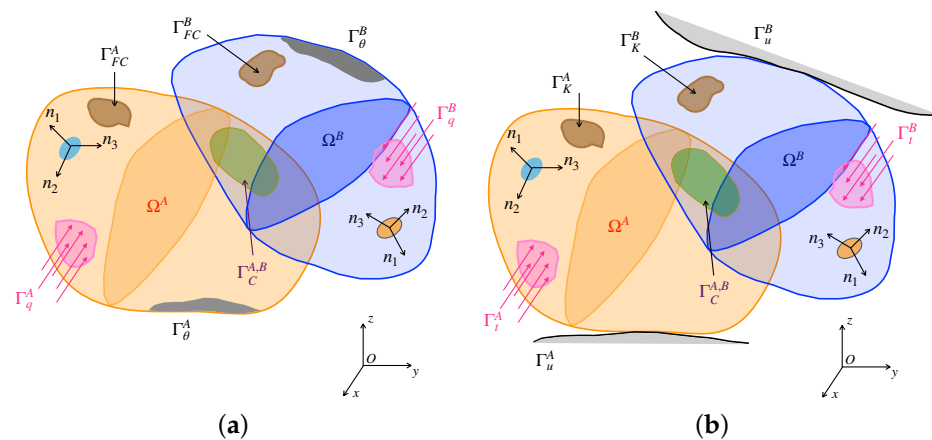


Figure 2. (a) Schema of the thermal problem. (b) Schema of the elastic problem.

The thermomechanical equilibrium equations of this problem under free volume heat sources and in the absence of body forces are:

$$\begin{aligned}
 k_t \theta_{,ii} &= 0 & \text{in } \Omega^l, \\
 \sigma_{ij,j} &= 0 & \text{in } \Omega^l,
 \end{aligned}
 \tag{1}$$

The thermal and elastic fields are coupled through the linear constitutive equation in Ω^l for isotropic thermoelasticity

$$\sigma_{ij} = \bar{\lambda} \varepsilon_{kk} \delta_{ij} + 2\bar{\mu} \varepsilon_{ij} - (3\bar{\lambda} + 2\bar{\mu}) \alpha_t (\theta - \theta_o) \delta_{ij},
 \tag{2}$$

where ε_{ij} is defined by

$$\varepsilon_{ij} = (u_{i,j} + u_{j,i})/2 \quad \text{in } \Omega^l.
 \tag{3}$$

Mechanical and thermal boundary conditions are prescribed on Γ^l . The Dirichlet boundary conditions are

$$\begin{aligned} \theta &= \bar{\theta} & \text{on } \Gamma_{\theta}^l \\ u_i &= \bar{u}_i & \text{on } \Gamma_u^l. \end{aligned} \tag{4}$$

and the Neumann boundary conditions are given by

$$\begin{aligned} q &= \bar{q} & \text{on } \Gamma_q^l \\ q &= \bar{h}_f(\bar{\theta}_f - \theta) & \text{on } \Gamma_{FC}^l \\ \sigma_{ij}n_{1j} &= \bar{t}_i & \text{on } \Gamma_t^l \\ \sigma_{ij}n_{1j} &= -\bar{K} \cdot u_i & \text{on } \Gamma_K^l, \end{aligned} \tag{5}$$

with \mathbf{n}_1 being the outward unit normal to the boundary (see Figure 2) and the heat flux q is defined as $q = q_i n_{1i}$, being $q_i = -k_i \partial_i \theta$.

3. Thermomechanical Contact Conditions

3.1. Thermal Contact Conditions

Nonlinear thermal boundary conditions on Γ_c can be defined, according to [6,16,18,25,26], for each solid as:

$$q^A = \frac{1}{R_{TC}} (\theta^B - \theta^A), \tag{6}$$

$$q^B = \frac{1}{R_{TC}} (\theta^A - \theta^B), \tag{7}$$

where R_{TC} is defined in Equation (9). The expressions above were derived from the energy balance for the contact interface Γ_c (i.e., $q^A + q^B = 0$), so the contact heat flux can be defined as: $q = q^A = -q^B$.

When two rough surfaces come into contact under the application of certain mechanical loads, a contact joint is created, formed by several microscopic contacts and microgaps, so that the real contact area is a small fraction of the apparent area, typically a few percent [34], heat flow from one surface to another overcomes a thermal contact resistance. According to [3,4,35–38], the thermal contact conductance is a function of several geometric, mechanical and thermal parameters such as: the surfaces roughness, the flatness of the surfaces, the surface microhardness, the thermal conductivities of both solids, the range of the contact tractions or the properties of the intermediate material.

Based on the works of Cooper [3] and works of Song and Yovanovich et al. [4,35–38], the general form of the contact conductance can be written as:

$$h_c = 1.25k_c \frac{m_c}{\sigma_c} \left(\frac{t_{n1}}{H_c} \right)^{0.95}, \tag{8}$$

where $k_c = 2k^A k^B / (k^A + k^B)$, $H_c = 2H^A H^B / (H^A + H^B)$, $\sigma_c = \sqrt{(\sigma^A)^2 + (\sigma^B)^2}$, $m_c = \sqrt{(m^A)^2 + (m^B)^2}$.

Once thermal contact conductance is obtained from Equation (8), the thermal contact resistance is modeled in Figure 3a and calculated as:

$$R_{TC} = \frac{1}{h_c}. \tag{9}$$

In the expressions above, it is assumed that the heat flows from one body to another only by means of conduction through the microcontacts (i.e., no interstitial conditions are considered) and no thermal interface material (TIM) is considered. Thus, to take into account both phenomena, the voids are filled with a TIM. The heat goes from one solid to the other by means of conduction through the microcontacts and throughout the microgaps (see Figure 4). According to [4,13,37,39], the gap conductance is modeled as:

$$h_g = \frac{k_g}{Y + M} \tag{10}$$

where the dependence of Y on the normal contact pressure is analyzed in [4,13,37,39] and it can be written as:

$$Y = 1.184\sigma_c \left[-\ln \left(3.132 \frac{p_n}{H_c} \right) \right]^{0.547} \tag{11}$$

M is a parameter that takes into account the rarefaction effects of a gas at high temperatures and low pressures. Therefore, according to [37], $M = 0$ if TIM is not a gas, and otherwise:

$$M = M_0 \frac{\theta_g P_{g0}}{\theta_0 t_{n1}} \tag{12}$$

where $\theta_g = (\theta^A + \theta^B)/2$.

Thus, the overall thermal contact conductance considering an interface material is calculated as:

$$h_{TC} = h_c + h_g \tag{13}$$

and consequently, $R_{TC} = \frac{1}{h_{TC}}$ as it is modeled in Figure 3b.

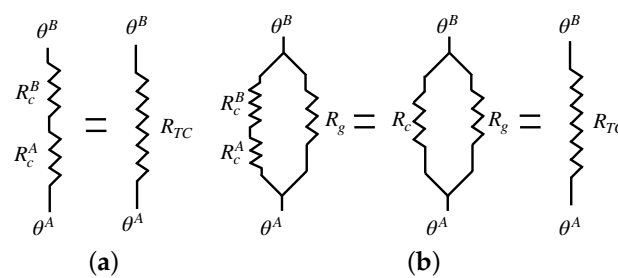


Figure 3. (a) Equivalent thermal contact resistance model for no TIM consideration. (b) Equivalent thermal contact resistance model for TIM consideration.

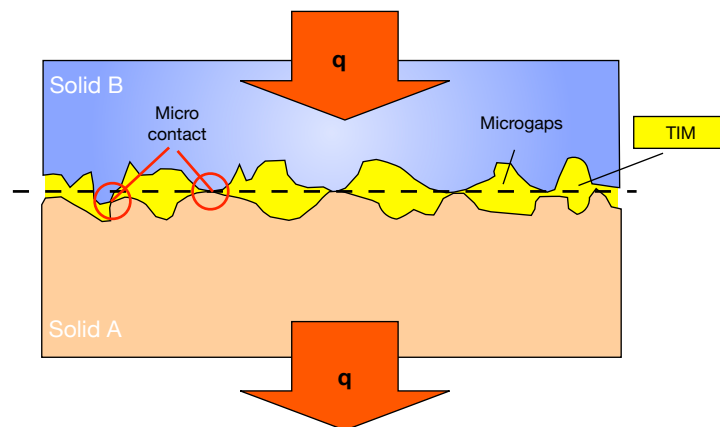


Figure 4. General thermal contact illustration and the schematic temperature distribution along the two bodies' contact surfaces.

On the other hand, in elements belonging to Γ_c that stay detached in the final solution, the following thermal conditions are imposed [23,27,28,40]:

- Vacuum conditions:

$$q^A = -q^B = 0. \tag{14}$$

- Convective conditions are divided in two:

- Forced convection:

$$q^l = h_f (\theta_f - \theta^l). \tag{15}$$

- Natural convection: A constant pseudo-resistance at these regions whose value is $R_{TC} = 2/h_f$ is considered. So the natural convection conditions are given by:

$$q^A = -q^B, \tag{16}$$

$$q^A = \frac{h_f}{2} (\theta^B - \theta^A). \tag{17}$$

- Conduction: The thermal jump depends on the separation between the pair of nodes ($g_n > 0$). In this case, it is equivalent to consider the influence of a variable thermal resistance whose value is $R_{TC} = k_f/g_n$.

$$q^A = -q^B, \tag{18}$$

$$q^A = \frac{k_f}{g_n} (\theta^B - \theta^A), \tag{19}$$

Finally, the boundary conditions on forced convection boundary, Γ_{FC} , are also considered as: $q^l = h_f (\theta_f - \theta^l)$.

3.2. Mechanical Contact Conditions

Under small displacement assumption, a common normal unit normal vector $\mathbf{n}_c = (\mathbf{n}^A - \mathbf{n}^B)/\|\mathbf{n}^A - \mathbf{n}^B\|$ is considered on Γ_c , as it is shown in Figure 5. Therefore, the nonlinear boundary conditions on the contact zone Γ_c are:

$$\sigma_{ij}n_{1j} = t_i \quad \text{on } \Gamma_c. \tag{20}$$

Under frictionless contact restrictions, the contact traction t_i on Equation (20) satisfies the Signorini's conditions on Γ_c :

$$g_n \geq 0, \quad t_n \leq 0, \quad g_n t_n = 0, \tag{21}$$

being $t_n = \mathbf{t} \cdot \mathbf{n}_c$, and $g_n = (g_o + u_n)$, $g_o = (\mathbf{x}^A - \mathbf{x}^B) \cdot \mathbf{n}_c$ (see Figure 5) and $u_n = (\mathbf{u}^A - \mathbf{u}^B) \cdot \mathbf{n}_c$.

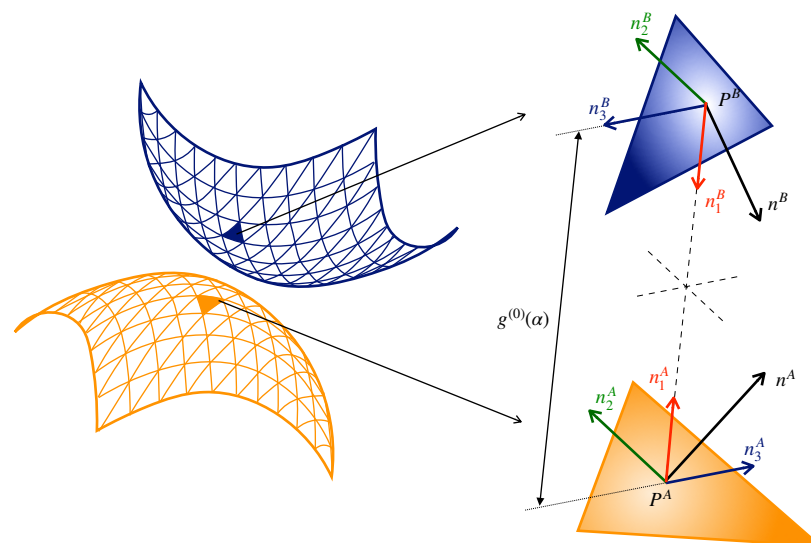


Figure 5. Local coordinate system of each pair of elements in contact.

4. Boundary Element Formulation and Contact Problem Approximation

4.1. Boundary Element Equations

The boundary integral equations for the 3D steady-state thermoelastic problem can be written for collocation points ξ and boundary points γ on Γ^l , according to Aliabadi [22], as:

$$c(\xi)\theta(\xi) + \int_{\Gamma} q^*(\xi, \gamma)\theta(\gamma) d\Gamma(\gamma) = \int_{\Gamma} \theta^*(\gamma, \xi)q(\gamma) d\Gamma(\gamma), \tag{22}$$

$$\begin{aligned} c_{ij}(\xi)u_j(\xi) - \int_{\Gamma} U_{ij}^*(\xi, \gamma)t_j(\gamma) d\Gamma(\gamma) + \int_{\Gamma} T_{ij}^*(\xi, \gamma)u_j(\gamma) d\Gamma(\gamma) = \\ = \int_{\Gamma} P_i^*(\xi, \gamma)\theta(\gamma) d\Gamma(\gamma) - \int_{\Gamma} Q_i^*(\xi, \gamma)q(\gamma) d\Gamma(\gamma), \end{aligned} \tag{23}$$

Equations (22) and (23) are discretized on Γ^l using triangular planar elements with the node located in the barycenter (see Figure 5), leading to a system of equations such as

$$\mathbf{Q}^l \boldsymbol{\theta}^l = \boldsymbol{\Theta}^l \mathbf{q}^l, \tag{24}$$

$$\mathbf{H}^l \mathbf{u}^l = \mathbf{G}^l \mathbf{t}^l + \bar{\mathbf{T}}^l \boldsymbol{\theta}^l - \bar{\mathbf{Q}}^l \mathbf{q}^l, \tag{25}$$

where vectors $\boldsymbol{\theta}^l$, \mathbf{q}^l , \mathbf{u}^l and \mathbf{t}^l contain the values of all nodal temperatures, heat fluxes, displacements and tractions, respectively, of solid Γ^l . Matrices \mathbf{Q}^l , $\boldsymbol{\Theta}^l$, \mathbf{H}^l , \mathbf{G}^l , $\bar{\mathbf{T}}^l$, $\bar{\mathbf{Q}}^l$ are the coefficients matrices containing the contributions from q^* , θ^* , U_{ij}^* , T_{ij}^* , P_i^* , Q_i^* respectively, and are calculated as:

$$\mathbf{Q}^l = \int_{A_k} q^*(\xi, \gamma) \partial A_k = \frac{-1}{4\pi} \int_{A_k} \frac{1}{r^2} \frac{dr}{dn} \partial A_k \tag{26}$$

$$\boldsymbol{\Theta}^l = \int_{A_k} \theta^*(\xi, \gamma) \partial A_k = \frac{1}{4\pi} \int_{A_k} \frac{1}{r} \partial A_k \tag{27}$$

$$\begin{aligned} \mathbf{H}^l &= \int_{A_k} T_{ij}^*(\xi, \gamma) \partial A_k = \\ &= \frac{-1}{8\pi(1-\nu)} \int_{A_k} \frac{1}{r^2} \{ [(1-2\nu)\delta_{ij} + 3r_i r_j] \frac{\partial r}{\partial n} - \\ &\quad - (1-2\nu)(r_i n_j - r_j n_i) \} \partial A_k \end{aligned} \tag{28}$$

$$\begin{aligned} \mathbf{G}^l &= \int_{A_k} U_{ij}^*(\xi, \gamma) \partial A_k = \\ &= \frac{1}{16\pi(1-\nu)G} \int_{A_k} \frac{1}{r} [(3-4\nu)\delta_{ij} + r_i r_j] \partial A_k \end{aligned} \tag{29}$$

$$\bar{\mathbf{T}}^l = \int_{A_k} P^*(\xi, \gamma) \partial A_k = \frac{\alpha(1+\nu)}{8\pi(1-\nu)} \int_{A_k} \frac{1}{r} (\delta_{ij} - r_i r_j) n_j \partial A_k \tag{30}$$

$$\bar{\mathbf{Q}}^l = \int_{A_k} Q^*(\xi, \gamma) \partial A_k = \frac{\alpha(1+\nu)}{8\pi(1-\nu)} \int_{A_k} r_i \partial A_k \tag{31}$$

being δ_{ij} the Kronecker's delta, r_i the vector $r(\xi, \gamma)$ that links the application point of the load ξ with the considered point γ , n_i is the component of the normal vector to the boundary, A_k is the area of the field element and $i, j = n_1, n_2, n_3$ are local axis directions (see Figure 2).

4.2. Thermoelastic Contact Discrete Formulation

The interface discretization on Γ_c , considering node-to-node contact, is performed for contact problems. Thus, each node on Γ_c^l creates a contact pair (I). Therefore, imposing

boundary conditions on Equations (24) and (25), the final discrete boundary equations passing the unknowns to the left-hand side, the final coupled systems for thermoelastic contact problems result in:

$$\mathbf{A}_{x_\theta}^l \mathbf{x}_\theta^l + \mathbf{A}_\theta^l \boldsymbol{\theta}_c^l + \mathbf{A}_q^l \mathbf{q}_c^l = \mathbf{b}_\theta^l, \quad (32)$$

where \mathbf{x}_θ^l collects the thermal nodal external unknowns (i.e., the nodal unknowns that are outside Γ_c). $\boldsymbol{\theta}_c^l$ and \mathbf{q}_c^l collect the thermal nodal unknowns at Γ_c^l . Finally, \mathbf{b}_θ^l collects the known nodal thermal boundary conditions.

$$\mathbf{A}_{x_e}^l \mathbf{x}_e^l + \mathbf{A}_u^l \mathbf{u}_c^l + \mathbf{A}_p^l \mathbf{t}_c^l = \mathbf{b}_e^l + \mathbf{b}_\theta^l. \quad (33)$$

being \mathbf{x}_e^l collect the elastic nodal external unknowns outside Γ_c . \mathbf{u}_c^l and \mathbf{t}_c^l are the mechanical nodal unknowns at Γ_c . Finally, \mathbf{b}_e^l collects the nodal mechanical boundary conditions known and \mathbf{b}_θ^l collects the normal thermal results obtained from Equation (32).

The previous systems of equations (Equations (24) and (25)) are solved following the double iterative procedure presented in [1,25].

5. Case Studies

The proposed formulation and the algorithms have been applied to study the thermomechanical behavior of low heat generation microelectronic packaging. The influence of simulating a retention mechanism at the top of the heatsink is analyzed. Moreover, the influence of the introduction of a thermal interface material at the contact zone between both solids on the thermomechanical variables of the packaging is also studied. Finally, the heat generation at the base of the microprocessor is increased in order to obtain the most efficient dissipation capacity for the improved architecture analyzed in this work.

The case studies presented in this work are organized as follows, starting from an initial geometry common to the three examples, successive modifications affecting the boundary conditions and/or the conditions at the interface between the microprocessor and the heatsink are proposed.

The resulting mechanical, thermomechanical and thermal results of the proposed modifications are, respectively, graphed and compared with the initial situation.

- Mechanical behavior
 - The differences obtained in the normal contact tractions are analyzed: tractions at the nodes located in the diagonal, in the whole contact zone and averages of normal contact tractions.
- Thermomechanical behavior
 - The differences obtained in the thermal contact resistance values are analyzed: tractions at the nodes located in the diagonal, in the whole contact zone and averages in thermal contact tractions.
- Thermal behavior
 - The maximum temperatures produced at the base of the microelectronic package are compared: temperatures at the nodes located in the diagonal, in the entire base of the microprocessor and the absolute maximum temperature.

A brief summary of what is going to be analyzed in the case studies herein presented is shown in Table 1. Moreover, additional figures are included in Appendix A.

Table 1. Case study summary.

Case	Initial Situation	Enhancements
1	<ul style="list-style-type: none"> Uniform clamping pressure is applied at the top face of the heatsink. The heatsink is simply supported on the micro-processor. 	<ul style="list-style-type: none"> The load is applied to the top face of the heatsink by means of an elastic retaining mechanism (variable clamping pressure). Heatsink edges are supported.
2	<ul style="list-style-type: none"> Vacuum conditions are assumed at the interface of the packaging. 	<ul style="list-style-type: none"> Thermal interface material is introduced at the interface of the packaging.
3	<ul style="list-style-type: none"> The heat generated at the base of the package is equivalent to a heat generation of 18.8 W. The convective coefficient is equal to 1000 W/°Cmm². 	<ul style="list-style-type: none"> The heat generation at the base is progressively increased. The convective coefficient of the cooling fluid is modified.

5.1. Effect of Retention MECHANISM at the Heatsink

In [1], the thermoelastic problem of a heatsink simply supported on the processor package was solved (see Figure 6a), obtaining the traction distribution in the contact zone and the maximum temperatures that were produced at the base of the microprocessor, when a uniform pressure was applied on the top face of the heatsink. It was observed that as a result of this arrangement, the normal traction distribution in the contact zone was not very uniform, leading to different tendencies: when the clamping pressures were low, the thermal effect predominated over the elastic one, so that these tractions were decreasing towards the edges of the encapsulation. For higher clamping pressures, the opposite effect occurred, with the normal contact tractions increasing as we moved away from the center. These non-uniform normal traction distributions affect significantly the thermal contact resistance at the interface and, in consequence, the final temperatures values at the contact zone. In addition, detachments are produced in the contact zone between the heat sink and the microchip.

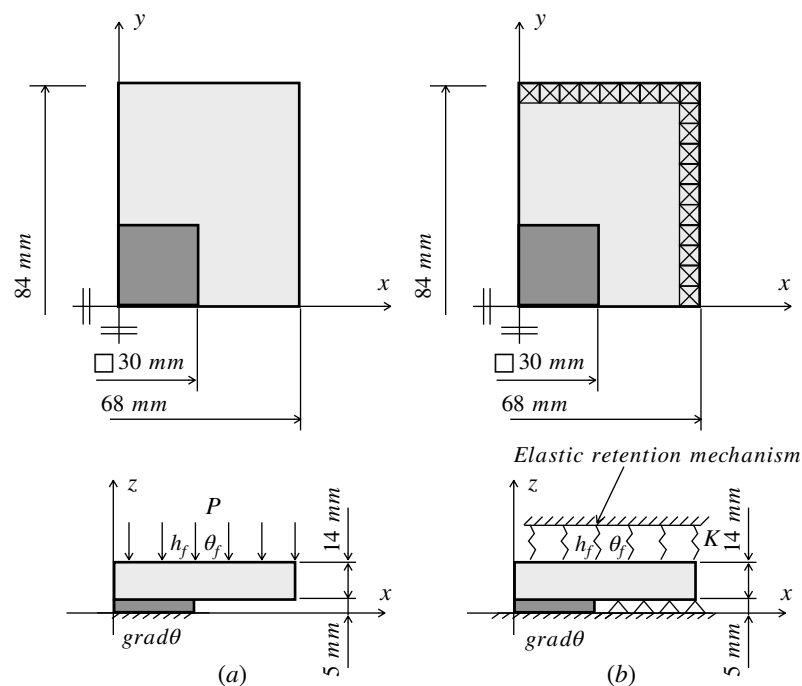


Figure 6. (a) Proposed geometry and initial boundary conditions. (b) New elastic boundary conditions.

In this example, the problem shown in Figure 6b is solved. The aim is to propose different improvements in the elastic boundary conditions to the heatsink and package assembly in order to improve the thermomechanical behavior of the packaging.

On the one hand, the clamping pressure is not kept uniform on the top face of the heatsink so the retention mechanism of the assembly is simulated by means of Winkler elastic support with a certain stiffness. Thus, a variable traction distribution is going to be produced depending on the deformation of the upper face of the heatsink. In order to perform the study, the different stiffness values of the Winkler elastic support were obtained from the average clamping pressures applied in each case (see Table 2). The results are going to be plotted and compared with the configuration shown in Figure 6a, where equivalent uniform clamping pressures are obtained.

Table 2. Equivalent Winkler elastic support stiffness.

Clamping Pressure [MPa]	K [MPa/mm]
0.1	90
0.15	150
0.2	250

On the other hand, the heatsink is supported on its boundary (see Figure 6a) in such a way as to limit the vertical movements of the heatsink edges in order to obtain a more uniform traction distribution in the contact area. This normal traction distribution is going to reduce the average thermal contact resistance in the contact zone, which is going to lead to an improvement in the heat dissipation.

The boundary conditions applied in the problem solved are described as follows and employed materials parameters are gathered in Table 3.

Table 3. Material properties of the microelectronic packaging.

	Processor	Heatsink
E [MPa]	275×10^3	70×10^3
ν	0.3	0.33
α [$^{\circ}\text{C}^{-1}$]	0.675×10^{-5}	2.3×10^{-5}
k [$\frac{\text{W}}{\text{C mm}}$]	20.9×10^{-3}	201×10^{-3}
H [MPa]	1207	1094
σ [mm]	1.14×10^{-6}	0.4×10^{-6}
m	0.1317	0.08648

- Elastic boundary conditions:
 - The perpendicular displacements are avoided ($u_{n_1} = 0$) at the lower face of the microprocessor ($z = 0$ mm);
 - On the rest of the faces, $t_{n_1} = t_{n_2} = t_{n_3} = 0$.
- Thermal boundary conditions:
 - The top surface of the aluminum heatsink ($z = 19$ mm) is assumed to be cooled by forced convection; ($\theta_f = 30$ $^{\circ}\text{C}$, $h_f = 10^{-3}$ W/mm^2 $^{\circ}\text{C}$)
 - The heat generated during operation of the processor is accounted for by treating the bottom surface ($z = 0$ mm) as a heat source (i.e., thermal gradient) with a total power of 18.8 W ($\text{grad}\theta = 1$ $^{\circ}\text{C}/\text{mm}$);
 - On the rest of the faces, $\text{grad}\theta = 0$.

In order to apply the BEM, different meshes have been tested to obtain satisfactory numerical solutions. The influence of different meshes in the contact thermomechanical variables is shown in Figure 7. The final discretization chosen is shown in Figure 8. The potential contact zone was discretized by 128 elements and the processor and the heatsink were meshed with 384 and 752 elements, respectively. Faces corresponding to planes YZ and XZ were not meshed since symmetry has been applied to those planes.

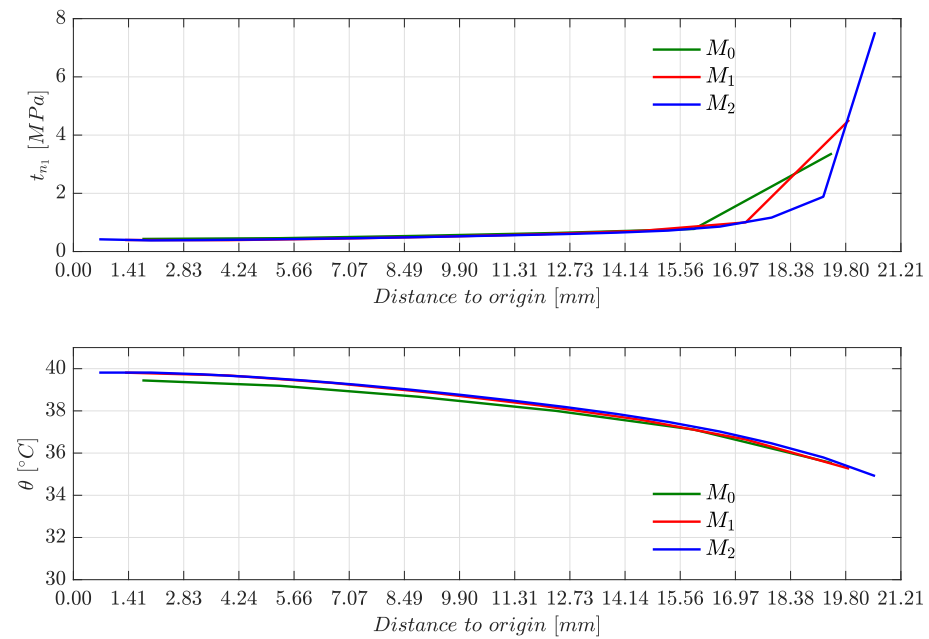


Figure 7. Discretization influence on the normal contact traction and temperature values at the nodes located at the diagonal of the contact zone for: $M_0 = 72$ elements, $M_1 = 128$ elements and $M_2 = 512$ elements.

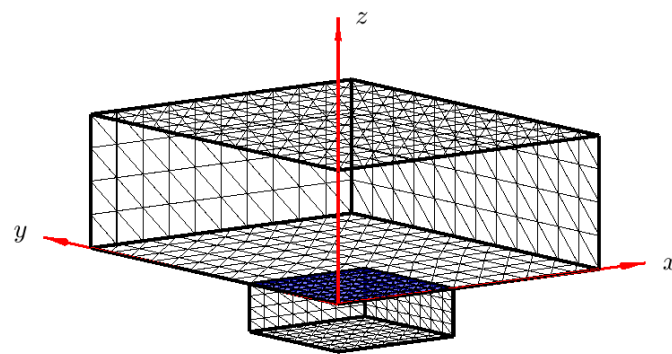


Figure 8. Microelectronic packaging boundary BEM mesh chosen.

Thermal conductance has been calculated using Equation (8) and parameters gathered in Table 3, obtaining $h_c = 7.650 \times 10^{-3} |t_{n1}|^{0.95} \text{ W}/^\circ\text{Cmm}^2$.

5.1.1. Mechanical Behavior

Figure 9 shows the normal traction distribution for the different uniform clamping pressures and for the different Winkler elastic support stiffness. The new elastic boundary conditions included in this work improve significantly the uniformity of the traction distribution in the contact for all the cases solved. For low clamping pressures, the mean normal traction increases in the contact zone (always less than 0.7 MPa) and the thermal contact resistance decreases (see Figure 10. Nevertheless, the average normal traction decreases in the contact zone for higher clamping pressures, as the elastic traction predominates over

the thermal traction. Thus, the supports located on the edges of the heatsink help to achieve a better distribution of the clamping pressure, relieving the microelectronic packaging. The stiffness of the Winkler elastic support should be less than $K = 150 \text{ MPa/mm}$ in order to avoid high tractions (greater than 0.7 MPa) that could damage the microelectronic packaging. For uniform clamping pressures lower than 0.07 MPa at the top of the heatsink, debonding occurred at the edges of the contact zone. In contrast, as the heatsink becomes longer than the processor, debonding occurred in the center of the contact zone when very high clamping pressures are applied. However, no debonding is produced in the contact zone when Winkler elastic supports are introduced since the traction distribution becomes more uniform. It has to be mentioned that due to the singularity at the edges, high tractions would appear at these locations whose exact values cannot be collected with the method used in this work [41,42]. These large traction values at the edges are going to produce small thermal contact resistance values and do not significantly affect the solution of the problem. Thus, it has been decided, for clarity, to not include them in Figure 9.

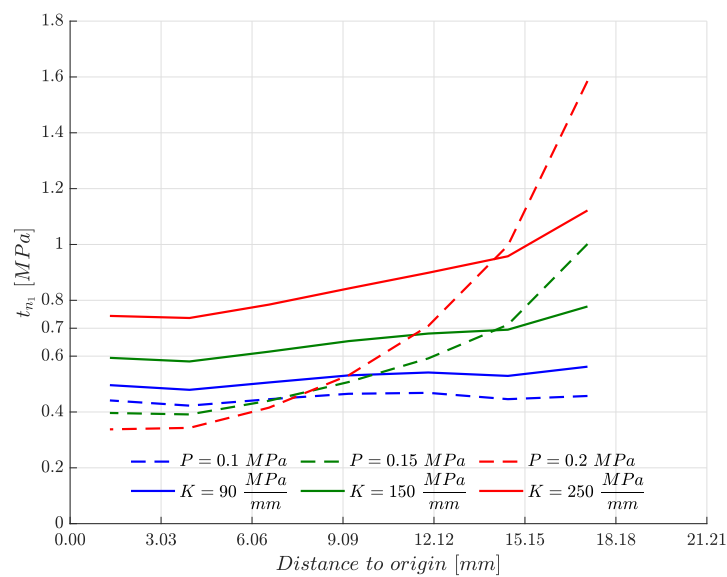


Figure 9. Normal contact traction distribution comparison at the nodes located at the diagonal of the contact zone for the uniform clamping pressure and Winkler elastic supports.

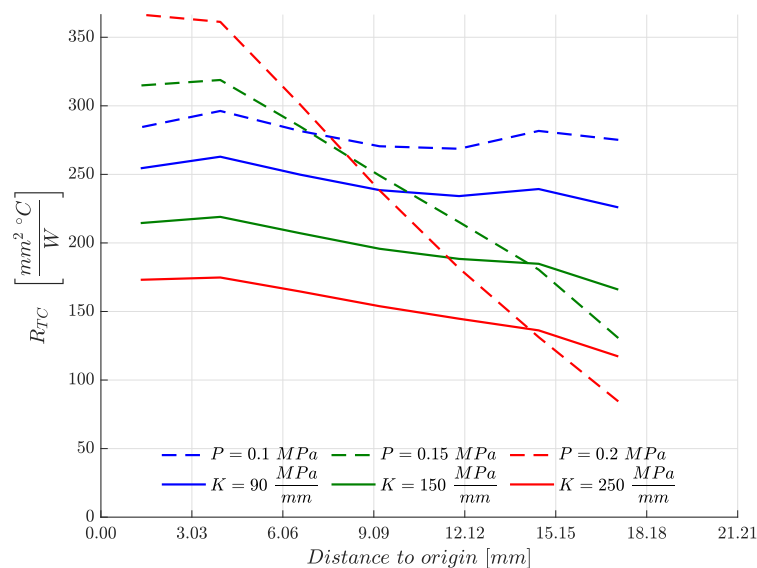


Figure 10. Thermal contact resistance comparison at the nodes located at diagonal of the contact zone for the uniform clamping pressure and Winkler elastic supports.

The complete normal traction distribution of the entire contact zone is shown in Figure A1 of Appendix A.1, where the abovementioned phenomenon of singularity at the edges can be observed. Moreover, Table 4 gathers the median contact normal traction comparison for different clamping pressures and different Winkler elastic support stiffness values.

Table 4. Median normal contact traction comparison for different uniform clamping pressures P and Winkler elastic support stiffness K .

P [MPa]	t_{n1} [MPa]	K [MPa/mm]	t_{n1} [MPa]
0.1	0.57	90	0.62
0.15	0.82	150	0.78
0.2	1.08	250	1.05

5.1.2. Thermomechanical Behavior

Figure 10 shows the thermal contact resistance values at the nodes located at the diagonal of the contact zone for different clamping pressures and Winkler elastic support stiffness. On the one hand, Figure A2 of Appendix A.1 shows the complete thermal contact resistance distribution comparison in the potential contact zone for the cases solved. A decrease and greater uniformity in thermal resistances is observed, resulting in better heat dissipation efficiency.

The median thermal contact resistance for each uniform clamping pressure and Winkler elastic support is gathered in Table 5.

Table 5. Median thermal contact resistance R_{TC} comparison for the uniform clamping pressure P and Winkler elastic supports stiffness K .

P [MPa]	R_{TC} [°Cmm ² /W]	K [MPa/mm]	R_{TC} [°Cmm ² /W]
0.1	257.75	90	228.84
0.15	208.29	150	182.31
0.2	189.83	250	139.15

5.1.3. Thermal Behavior

This improvement leads to a smooth descent of the maximum temperatures at the base of the microprocessor and in a more uniform distribution, as shown in Figure 11 and in Table 6.

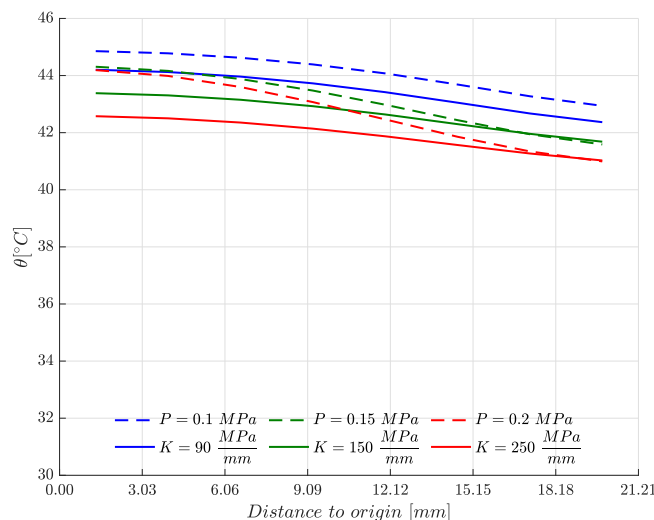


Figure 11. Temperature distribution comparison at the elements located at the diagonal of the base of the microprocessor for the uniform clamping pressure and Winkler elastic supports.

Table 6. Maximum temperature θ at the base of the microprocessor comparison for the uniform clamping pressure P and Winkler elastic supports stiffness K .

P [MPa]	θ [°C]	K [MPa/mm]	θ [°C]
0.1	44.85	90	44.20
0.15	44.31	150	43.38
0.2	44.19	250	42.58

On the one hand, Figure A3 of Appendix A.1 shows the complete temperature distribution of the base of the microprocessor. The descent and the more uniform distribution of the temperatures as the Winkler elastic support stiffness increases can be clearly seen.

Finally, the complete temperature distribution at the boundary of the microelectronic packaging for the uniform clamping pressure ($P = 0.15$ MPa) is shown in Figure A4 of Appendix A.1.

5.2. Influence of the Inclusion of a Thermal Interface Material on the Contact Thermomechanical Variables

In the previous example in Section 5.1 and in [1], a theoretical problem was simulated in which vacuum conditions were assumed at the interface between the microprocessor and the heatsink, so the heat transfer occurred only through the microcontacts. In reality, the microgaps are filled with an intermediate thermal material (TIM), so the thermal contact resistance decreases significantly compared to the thermal contact resistance when vacuum conditions are assumed. Thus, TIMs are used to provide an effective heat conduction path between both surfaces since the heat transfer is produced through both microcontacts and TIM. In this example, the influence of the introduction of a TIM in the thermomechanical variables in low heat generation microelectronic packaging is analyzed. Geometry used and new boundary conditions are shown in Figure 12. The heatsink is considered to be under the influence of retention Winkler elastic support with stiffness $K = 150$ MPa/mm and it is also considered to be supported at the edges. Moreover, mesh and material properties are the same as in the previous example. The thermal contact resistance (R_{TC}) takes into account the existence of different TIMs filling the microgaps by means of Equations (8), (10) and (13) using the parameters gathered in Table 7.

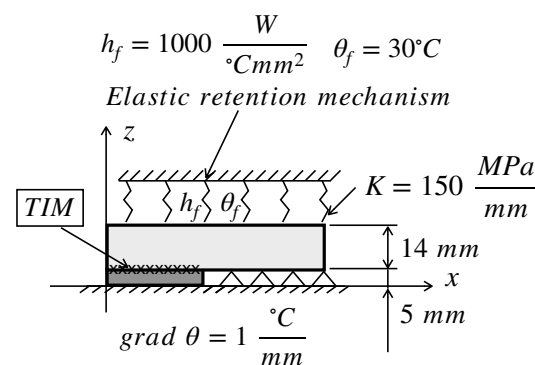


Figure 12. Model analyzed in this example where the influence of different TIMs is analyzed.

Table 7. Thermal interface material properties used to calculate the thermal contact resistance (R_{TC}).

TIM	k [W/mm°C]	M_0 [mm]
Air	0.026×10^{-3}	0.373×10^{-3}
Helio	0.15×10^{-3}	2.05×10^{-3}
Grease	0.7×10^{-3}	0.0

5.2.1. Mechanical Behavior

Figure 13a,b show that the normal contact traction distribution is not greatly affected by the inclusion of the TIM. A slight decrease in the normal contact traction values is produced as the conductivity of the TIM increases.

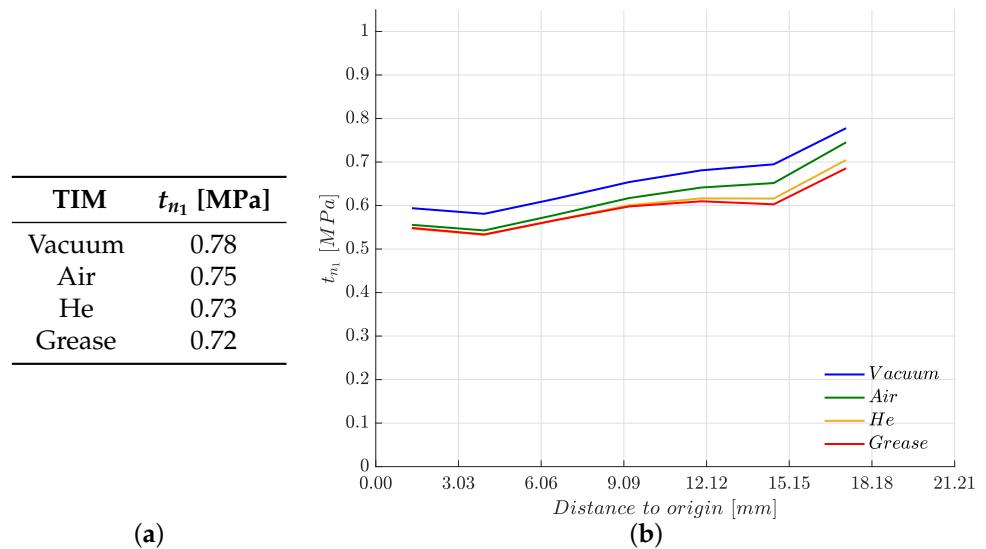


Figure 13. (a) Median normal contact traction value comparison at the potential contact zone. (b) Normal contact traction distribution comparison at the nodes located at the diagonal of the contact zone.

The clamping pressure is barely important to improve heat dissipation of the packaging when grease is introduced at the interface. This pressure should have minimum values to ensure contact between the microprocessor and the heatsink in addition to maximum values to avoid large stresses in the microelectronic packaging. Finally, Figure A5 of Appendix A.2 presents the complete normal contact traction distribution in the potential contact zone for all the different TIMs analyzed.

5.2.2. Thermomechanical Behavior

The thermal contact resistance values is the most thermomechanical parameter affected as it is shown in Figure 14. The thermal contact resistance values are significantly improved due to the reduction of microgaps in the interstitial zone between both solids, which are fulfilled by the TIM. Opposite to the normal contact traction values, thermal contact resistance values decrease as the conductivity of the TIM increases. In addition, Figure A6 of Appendix A.2 shows how thermal contact resistances become more uniform as the conductivity of the TIM increases, with a minor dependency with the normal contact traction values.

For the case of the microgaps filled by air, the values of thermal conductance in the microcontacts are of the same order as the values of the thermal conductance of a gas. Conversely, the thermal conductance of the microcontacts is negligible compared to the thermal conductance of the TIM when the microgaps are fulfilled by grease, as it is shown in Figure 15 and in Table 8.

Table 8. Median microcontacts thermal contact conductance (h_c [$W/^\circ Cmm^2$]) and TIM thermal conductance (h_g [$W/^\circ Cmm^2$]) comparison for all TIMs studied calculated according to Equations (8) and (10).

	$h_{c,median}$	$h_{g,median}$	$h_{TC,median}$	$R_{TC,median}$
Vacuum	5.485×10^{-3}	-	5.485×10^{-3}	182.31
Air	5.485×10^{-3}	6.502×10^{-3}	1.1987×10^{-2}	83.42
Helium	5.485×10^{-3}	3.6218×10^{-2}	4.1668×10^{-2}	24.00
Grease	5.485×10^{-3}	0.1787	0.1842	5.43

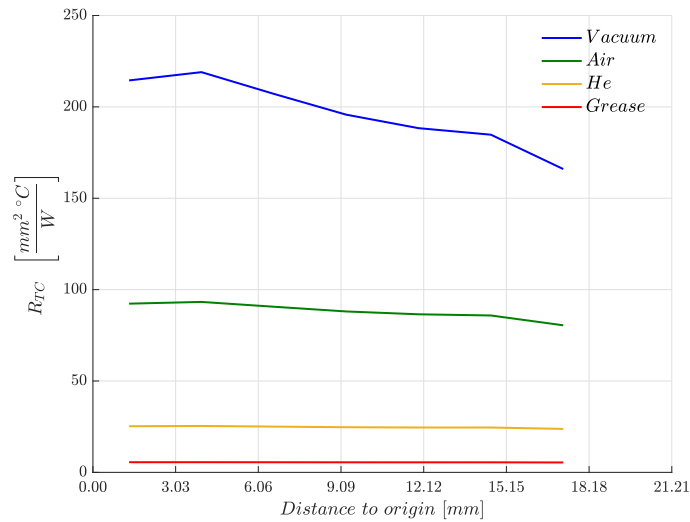


Figure 14. Thermal contact resistance distribution comparison at the nodes located at the diagonal of the contact zone.

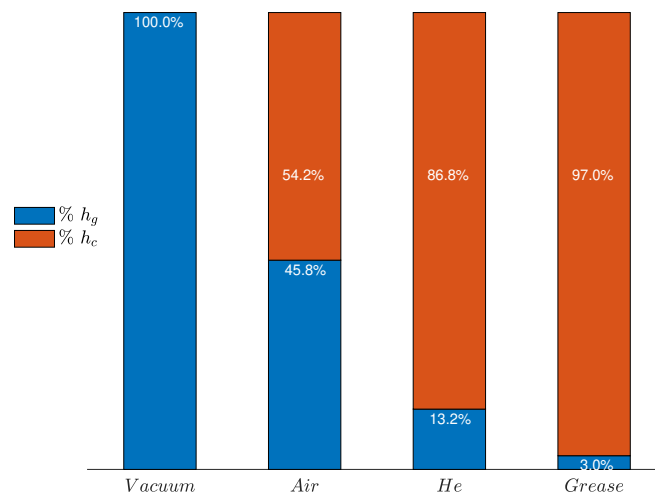


Figure 15. Microcontacts thermal contact conductance (h_c) and TIM thermal conductance (h_g) % comparison for all TIMs studied at the potential contact zone.

5.2.3. Thermal Behavior

In relation to the thermal behavior, perfect contact is also assumed in order to analyze the efficiency of filling the microgaps with TIM (see Table 9). As a consequence of the decrease of the thermal contact resistance as the conductivity of the TIM increases, the maximum temperatures in the packaging decrease, as it is shown in Figure 16a. When a thermal grease is included in the interface of both solids, the temperature distribution at the base of the microprocessor becomes very close to the ideal situation that no thermal contact resistance is produced in the contact zone (perfect contact conditions), as it is also shown in Figure 16b.

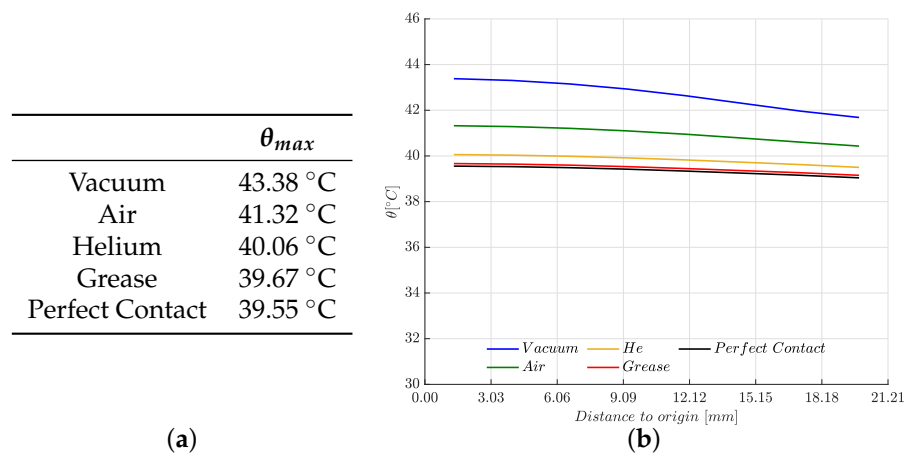


Figure 16. (a) Maximum temperature values comparison on the base of the microprocessor for each TIM analyzed. (b) Temperature distribution comparison at the nodes located at the diagonal of the base of the microprocessor.

Moreover, Figure A7 of Appendix A.2 shows the complete temperature distribution of the base on the microprocessor of the microelectronic packaging for all the TIM types studied.

Defining the efficiency (E_i) as:

$$E_i = \frac{(\theta_{vacumm} - \theta_i)}{(\theta_{vacumm} - \theta_0)} \tag{34}$$

where θ_{vacumm} is the maximum interface temperature for vacuum conditions, θ_i is the maximum temperature for each TIM analyzed and θ_0 is the maximum interface temperature for perfect contact conditions.

Table 9. Microelectronic packaging thermal efficiency for each TIM analyzed.

	θ_i	E_i
Vacuum	43.38 °C	0.00%
Air	41.32 °C	53.80%
Helium	40.06 °C	86.70%
Grease	39.67 °C	97.00%
Perfect Contact	39.55 °C	100.00%

Finally, Figure A8 of Appendix A.2 illustrates the temperature distribution on the boundary of both microprocessor and heatsink when the interface between both solids is filled by a thermal grease.

5.3. Microelectronic Packaging Behavior under Higher Heat Generation at the Microprocessor

In this example, the behavior of the heatsink–microprocessor assembly is simulated by increasing the heat generation at the base of the microprocessor in order to obtain the maximum efficient dissipation capacity for the improved architecture analyzed in previous example in Section 5.2.

As the heat generated in the CPU core increases, the normal traction in the contact zone also increases. In order to avoid high stresses on the microprocessor, the stiffness of the retention mechanism will have to be varied in order to avoid these stresses and also to ensure contact across the interface.

Geometry, mesh, boundary conditions and material properties are the same as in the previous example in Section 5.2 including a thermal grease at the interface of the microelectronic packaging, as shown in Figure 17.

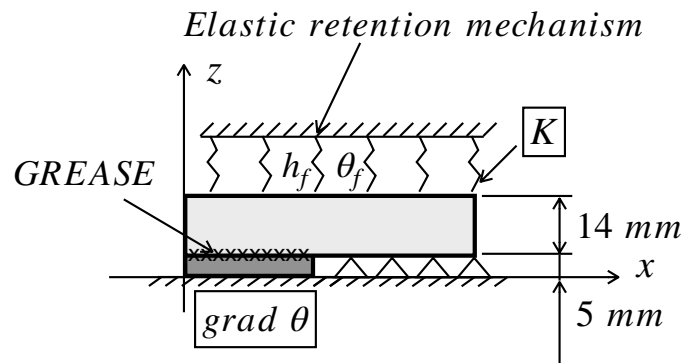


Figure 17. Model analyzed in this example where a thermal grease is introduced at the interface and the effect of different Winkler elastic support stiffness K and $grad\theta$ is analyzed.

Firstly, for each heat generation value, the maximum stiffness of the retention mechanism will be obtained so that the normal contact traction on the microchip are close to 0.7 MPa. The cases studied are gathered in Table 10.

Table 10. Heat q [W] generated at the base of the microprocessor and its respective maximum Winkler elastic support stiffness.

$grad\theta$ ($^{\circ}C/mm$)	q (W)	K (MPa/mm)
1.00	18.81	150
1.50	28.22	75
2.00	37.62	10
2.50	47.03	—

where the heat generated at the base of the microprocessor is calculated as follows: $q = k \cdot A \cdot grad\theta$. Being k and A the thermal conductivity and the area of the microprocessor, respectively.

5.3.1. Mechanical Behavior

Figure 18 shows how the normal contact traction distribution changes as heat generated increases and the stiffness of the retaining mechanism decreases (see Table 10). This occurs because thermal deformations have a greater predominance than the elastic deformations. Normal contact traction distributions are initially increasing functions with a maximum at the edge and then, they reverse this tendency and tend to detachments at locations further from the contact zone center.

With the method herein used, it is possible to quantify the maximum stiffness that the mechanism can have so that the normal contact tractions do not exceed 0.7 MPa, as well as the limit of the heat generation that can be dissipated efficiently (without debondings at the contact zone) for this architecture, which is approximately 40 W. For higher heat generation, it is not possible to obtain a normal contact traction distribution that does not exceed 0.7 MPa in areas close to the center of the microchip.

It is observed that when medium heat generation (50 W) is simulated, the normal traction distribution is not affected by the stiffness of the system (which is very small). Therefore, it is not possible to design a retention mechanism that ensures both tractions lower than 0.7 MPa and detachments between the heatsink and the microprocessor. For these cases, it is necessary to use different configurations that dissipate better the heat generated at the microchip.

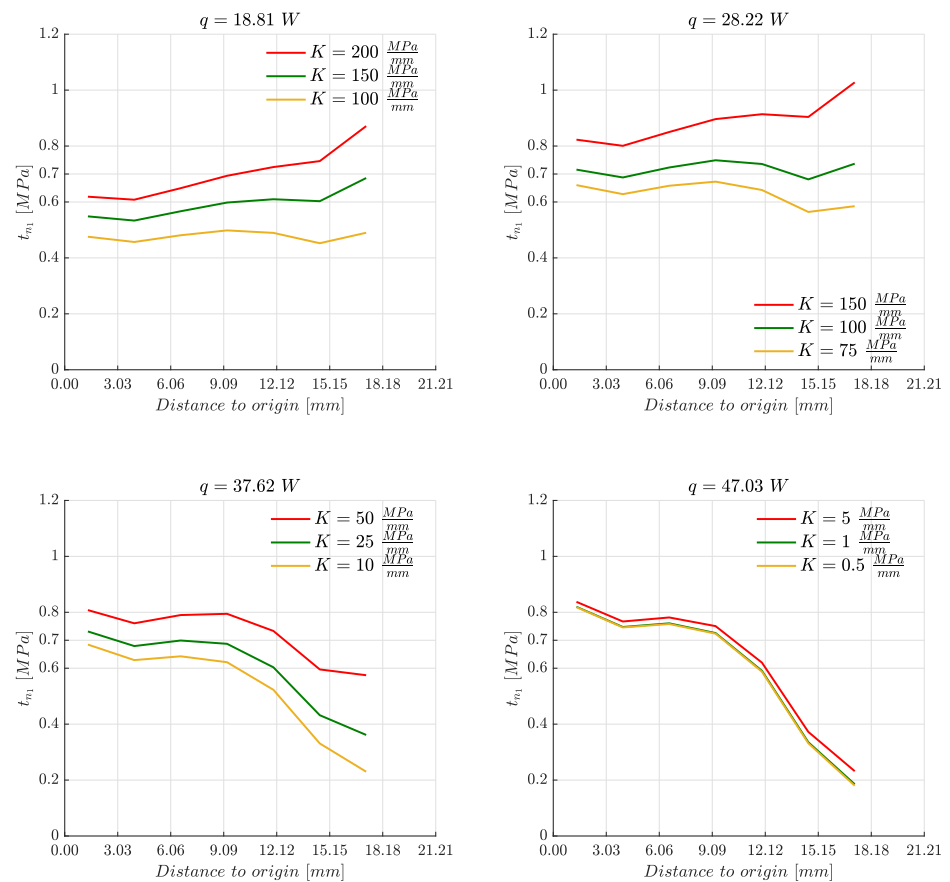


Figure 18. Normal traction distribution at the nodes located at the diagonal of the contact zone of all the stiffness of the retaining mechanism analyzed for: $q = 18.81$ W, $q = 28.22$ W, $q = 37.62$ W and $q = 47.03$ W.

5.3.2. Thermal Behavior

On the other hand, Figure 19 shows the temperature distribution at the nodes located at the diagonal. It is shown that the final temperatures barely depend on the stiffness of the retention mechanism since the heat transfer is mainly produced by the thermal grease. In addition, they remain practically constant, varying a little more as heat dissipation becomes less effective. Figure A9 of Appendix A.3 presents the complete temperature distribution at the base of the microprocessor for all the heat generation values studied.

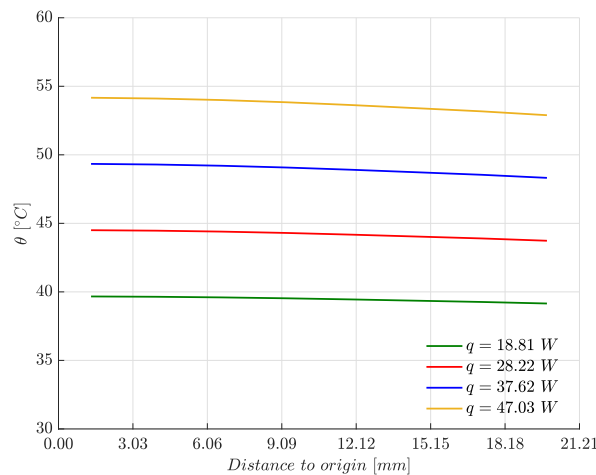


Figure 19. Temperature distribution at the nodes located at the diagonal of the base of the microprocessor for: $q = 18.81$ W, $q = 28.22$ W, $q = 37.62$ W and $q = 47.03$ W

The maximum temperature values for all the heat generation values analyzed obtained at the base of the microelectronic packaging are shown in Figure 20.

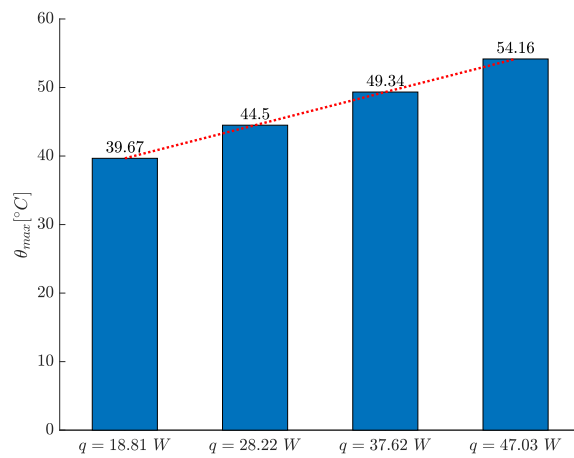


Figure 20. Maximum temperature at the base of the microprocessor for: $q = 18.81$ W, $q = 28.22$ W, $q = 37.62$ W and $q = 47.03$ W.

When a thermal grease is introduced at the interface between both solids, the contact is almost perfect. Therefore, the maximum temperatures could be obtained as a linear function of the microprocessor power.

$$\theta_{max} = C(h_f, \theta_f) \cdot q + \theta_f \tag{35}$$

where C is the coefficient that depends on the convective coefficient (h_f [W/mm²°C]) and the temperature (θ_f [°C]) of the cooling fluid and q [W] is the heat generated by the microchip.

Solving the modeled geometry when $\theta_f = 30$ °C for different values of h_∞ yields the results presented in Figure 21

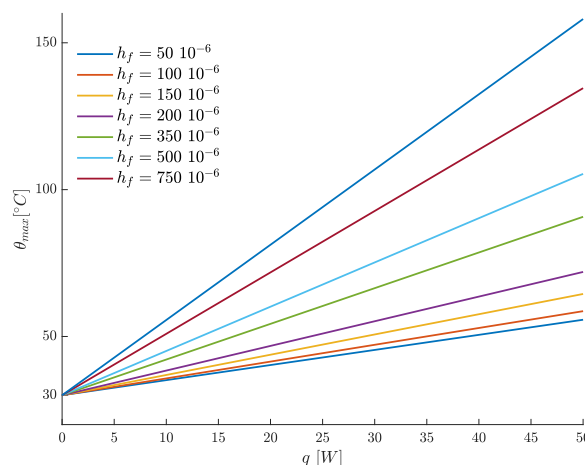


Figure 21. Maximum temperature at the base of the microprocessor for different values of $h_f \left[\frac{W}{\text{°Cmm}^2} \right]$.

From the lines shown in Figure 21, correlation C (slope of each line as function of h_f) can be obtained approximately: $C = 0.00897 \cdot h_f^{-0.5783}$, as shown in Figure 22.

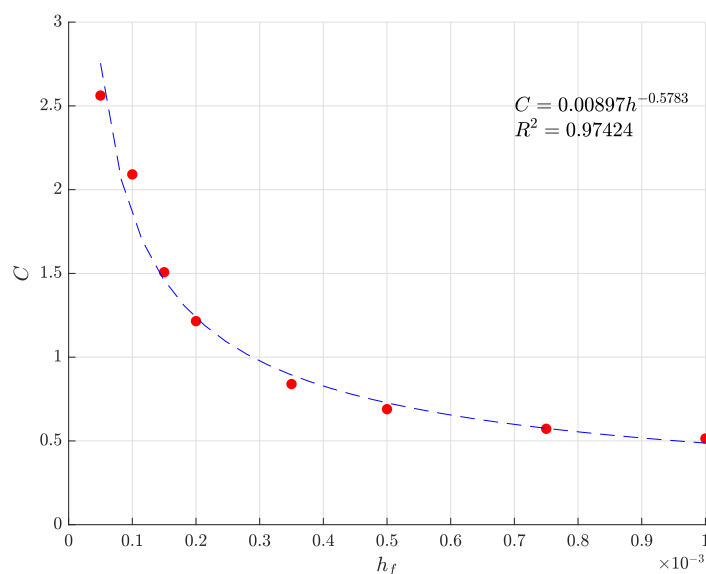


Figure 22. C correlation as a function of h_f .

6. Conclusions

In this work, a simulation based on the BEM in order to optimize the thermomechanical behavior of the microelectronic packaging for medium-low heat generation is presented. The cooling capacity of the microelectronic packaging was improved, supporting the edges of the heatsink and also replacing the constant clamping pressure applied on the top face of the heatsink by a retention mechanism simulated by means of Winkler elastic supports. In addition, a thermal interface material is introduced at the interface between both solids of the microelectronic packaging in order to improve the thermal contact conductance. The nonlinearity inherent in the problem due to the thermal contact conductance is solved by means of a double iterative procedure. The thermomechanical variables are obtained in a few iteration with the formulation proposed in this work. Following these studies, the main conclusions and remarks of this work are:

- Elastic boundary conditions modifications:
 - Supporting the edges of the heatsink minimizes the cantiliver effects produced. Therefore, the planarity is improved and a more uniform normal contact traction distribution in the contact zone is produced;
 - Replacing the heatsink clamping pressure by a retention mechanism also improves the uniformity of the normal contact traction distribution in the contact zone and possible detachments at the contact zone are avoided. Moreover, as shown in Figure 10 and in Table 5, the retention mechanism reduced the thermal contact resistance for the equivalent constant clamping pressure. Thus, the cooling capacity of the complete packaging increases;
- Modifications at the contact zone:
 - The thermal contact conductance is greatly improved by the inclusion of a TIM. The thermal contact resistance is reduced as the thermal conductivity of the TIM, so the maximum temperatures of the packaging decreases;
 - Thermal grease filling the microgaps produced a thermal efficiency of the microelectronic packaging very close to the ideal situation in which no thermal contact resistance is produced (see Table 9);
 - When a thermal grease is introduced at the interface between both solids, the contact is almost perfect.

Finally, the proposed method simulates satisfactorily the thermomechanical behavior of the heatsink–microprocessor assembly for the proposed improved architecture when heat generations are medium-low. However, this formulation cannot be also applied to analyze the thermomechanical contact problem for medium-high heat generation microelectronic packaging. In order to obtain a greater heat dissipation efficiency in this type of packaging, the contact area has to increase, and therefore, so does the heat dissipation area. This would be the result of incorporating an intermediate element that encapsulates the microprocessor, called Integrated Head Spreader (IHS), whose function is to capture the heat generated by the CPU core and distribute it over a wider area and then transfer it to the heatsink (see Figure 23). Therefore, it is going to exit two different contact zones. Moreover, the simulation of heatpipes running through the heatsink in order to capture the CPU heat and distribute it better throughout the block could also improve the heat dissipation efficiency.

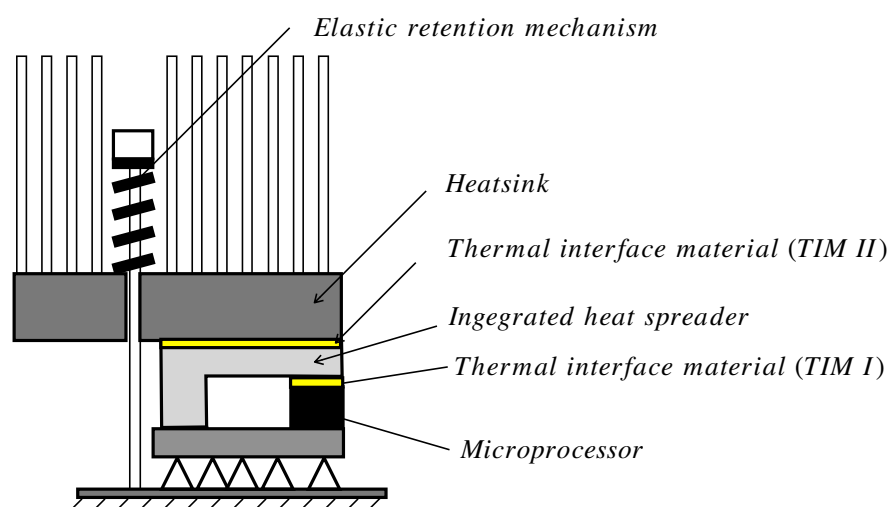


Figure 23. Possible microelectronic packaging architecture for high-generation conditions.

Author Contributions: Conceptualization, J.V.-E., J.C.-R. and I.U.-M.; Formal analysis, J.V.-E., J.C.-R. and I.U.-M.; Investigation, J.V.-E., J.C.-R., V.G.-P. and I.U.-M.; Methodology, J.V.-E., J.C.-R. and I.U.-M.; Software, J.V.-E., J.C.-R., V.G.-P. and I.U.-M.; Supervision, J.V.-E., J.C.-R. and I.U.-M.; Validation, J.V.-E. and I.U.-M.; Writing—original draft, J.V.-E., J.C.-R. and I.U.-M.; Writing—review & editing, J.V.-E., J.C.-R., V.G.-P. and I.U.-M. All authors have read and agreed to the published version of the manuscript.

Funding: This research received no external funding.

Institutional Review Board Statement: Not applicable.

Informed Consent Statement: Not applicable.

Data Availability Statement: The authors confirm that the data supporting the findings of this study are available within the article. Furthermore, if any additional data be required, they are available upon reasonable request to the corresponding author.

Conflicts of Interest: The authors declare no conflict of interest.

Nomenclature

α_t	thermal dilatation coefficient
$c(\xi)$	boundary integral equation thermal free term
$c_{ij}(\xi)$	boundary integral equation elastic free term
ϵ_{ij}	infinitesimal strain tensor
γ	boundary point
Γ^l ($l = A, B$)	solids boundary
H_c	harmonic mean surface microhardness
g_0	initial gap between the bodies
h_c	contact conductance
h_f	fluid convective coefficient
h_{TC}	thermal contact conductance
k_c	harmonic mean thermal conductivity of the interface
k_g	TIM thermal conductivity
K	Winkler elastic supports stiffness
k	thermal conductivity
$\tilde{\lambda}, \tilde{\mu}$	Lamé coefficients
m_c	effective mean absolute asperity slope
M	parameter of a gas at high temperatures
M_0	reference gas parameter at temperature θ_0
\mathbf{n}_1	outward unit normal to the boundary
Ω^l ($l = A, B$)	solids in contact
P_{g0}	pressure of the gas at the interface
$P_i^*(\xi, \gamma)$	vector derived from the consideration of thermal deformations
$Q_i^*(\xi, \gamma)$	vector derived from the consideration of thermal deformations
q	heat flux
$q^*(\xi, \gamma)$	fundamental solution for thermoelastic problem
$\theta^*(\xi, \gamma)$	fundamental solution for thermoelastic problem
$T_{ij}^*(\xi, \gamma)$	fundamental solution for thermoelastic problem
$U_{ij}^*(\xi, \gamma)$	fundamental solution for thermoelastic problem
R_{TC}	contact thermal resistance
σ_{ij}	Cauchy stress tensor
σ_c	effective RMS surface roughness
RMS	Root mean square
TIM	thermal interface material
t_i	tractions vector
t_{n_1}	normal contact traction
θ	temperature
θ_0	reference temperature
θ_g	temperature of the gas at the interface
θ_f	temperature of fluid
u_i	displacements vector
u_n	relative displacement
Y	effective height of the cavity

Appendix A. Additional Figures

Additional figures for a better understanding are included in this section for the three cases of study analyzed.

Appendix A.1. Case of Study 1

In this section, additional figures are included for case study 1. The complete distributions of normal tractions, thermal contact resistances and temperatures in the contact zone are shown. As well as, the temperature distribution at the boundary of the microelectronic packaging.

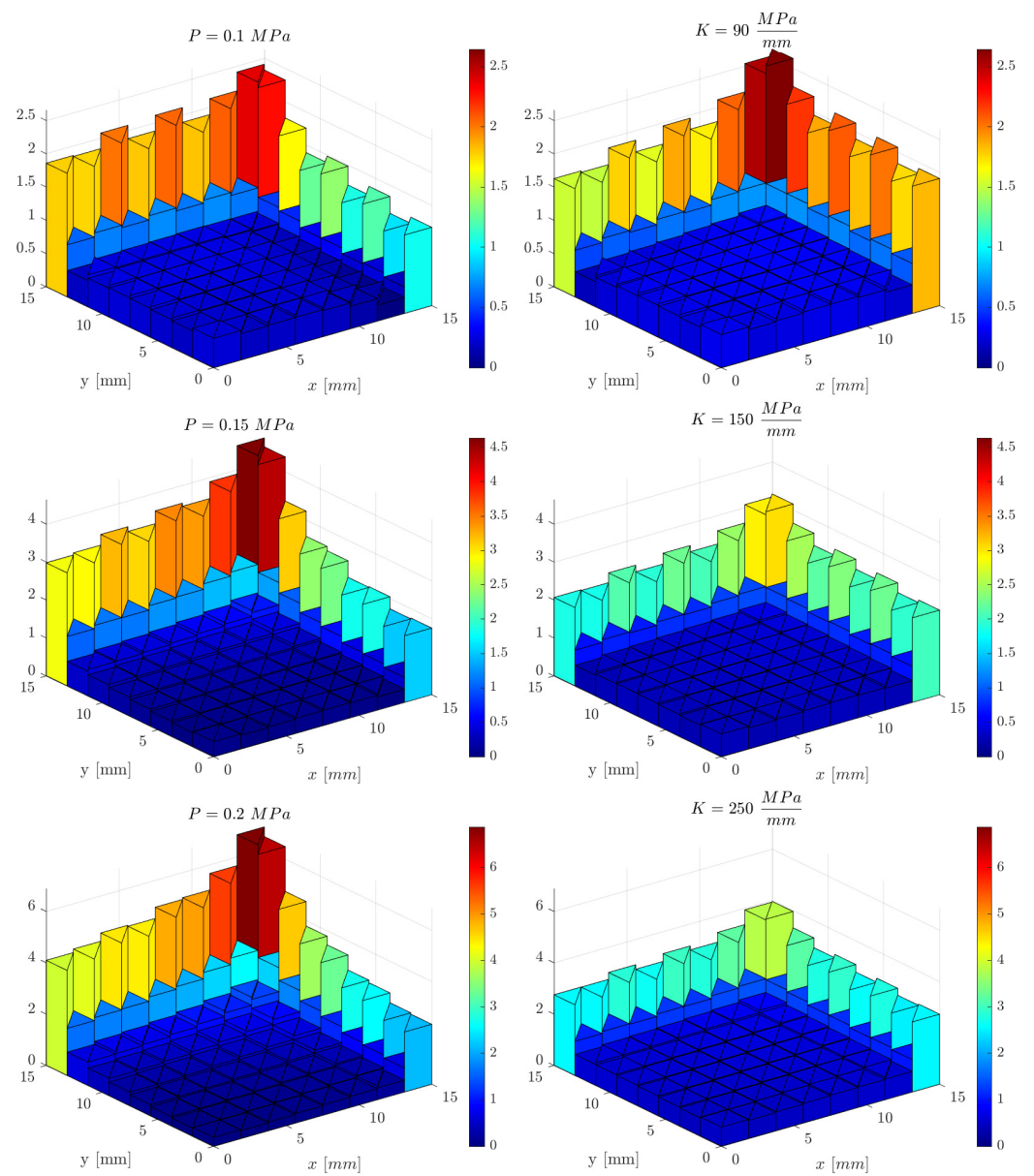


Figure A1. Complete normal contact traction (t_{n_1} [MPa]) distribution comparison at the contact zone for the uniform clamping pressure and Winkler elastic supports.

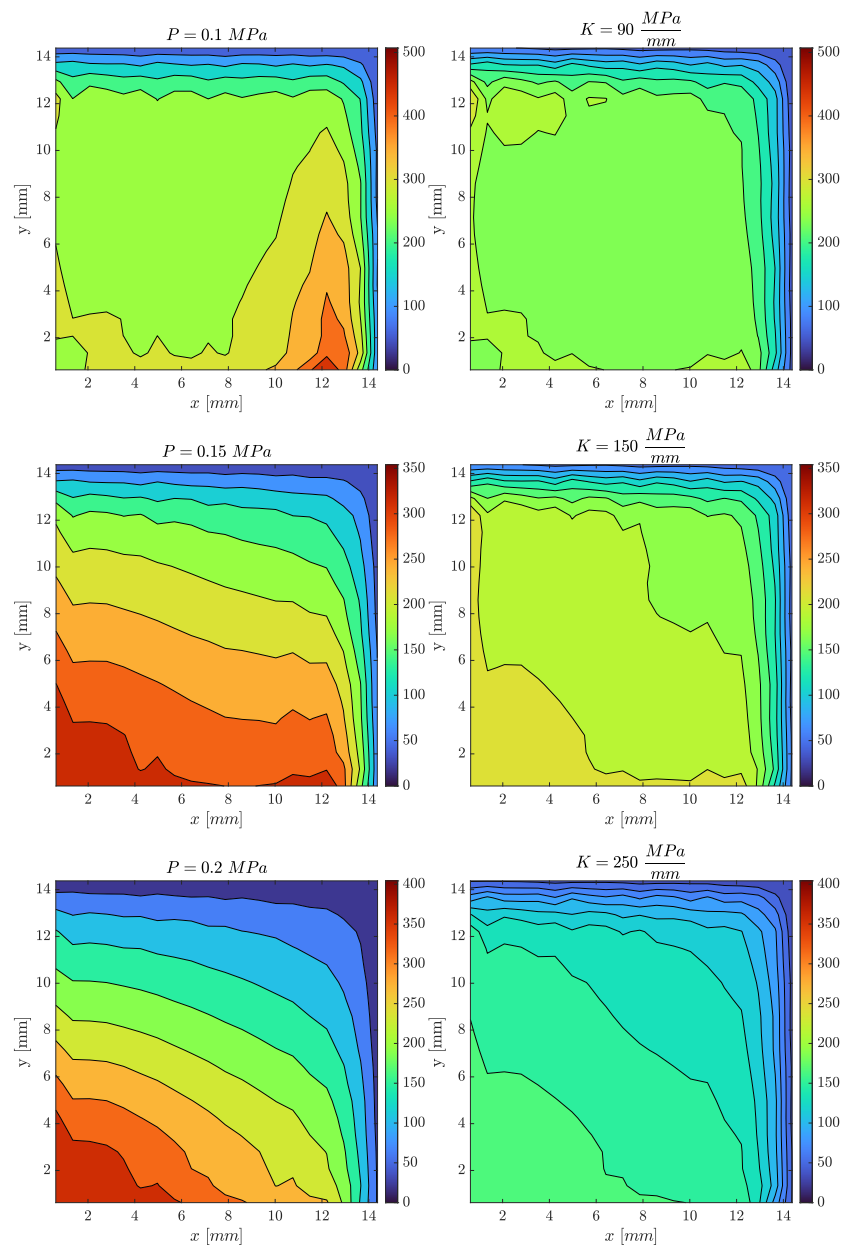


Figure A2. Complete thermal contact resistance R_{TC} [$^{\circ}\text{Cmm}^2/\text{W}$] distribution comparison in the potential contact zone for the uniform clamping pressure and Winkler elastic supports.

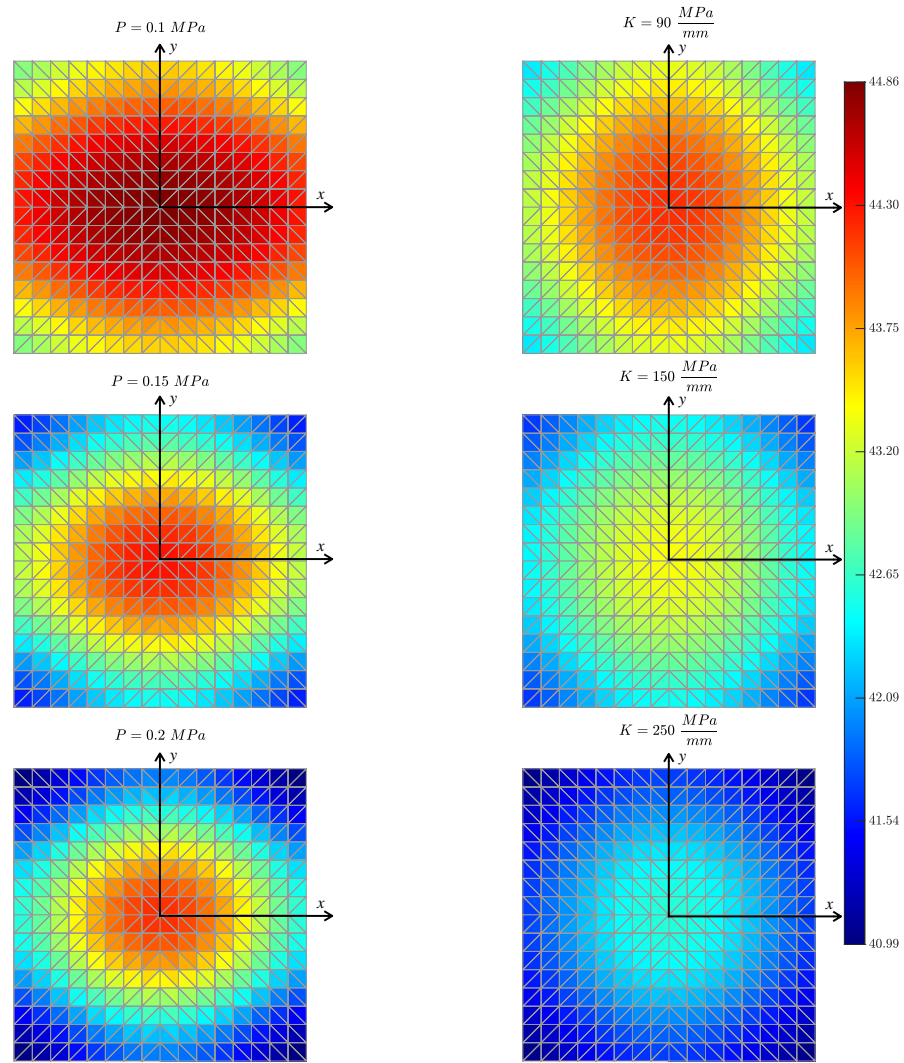


Figure A3. Complete temperature distribution (θ [°C]) comparison at the base of the microprocessor for the uniform clamping pressure and Winkler elastic supports.

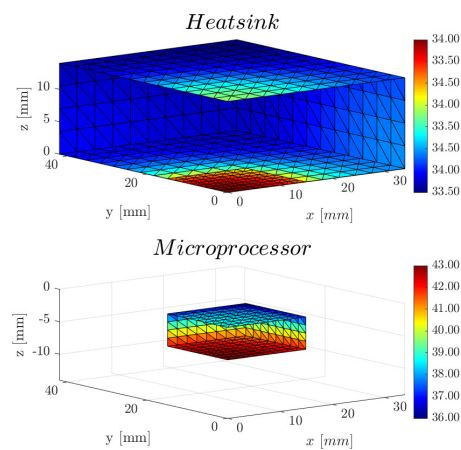


Figure A4. Temperature (θ [°C]) distribution on the boundary of the microelectronic packaging for $P = 0.15$ MPa.

Appendix A.2. Case of Study 2

In this section, additional figures are included for case study 2. The complete distributions of normal tractions, thermal contact resistances and temperatures in the contact zone

are shown. As well as, the temperature distribution at the boundary of the microelectronic packaging.

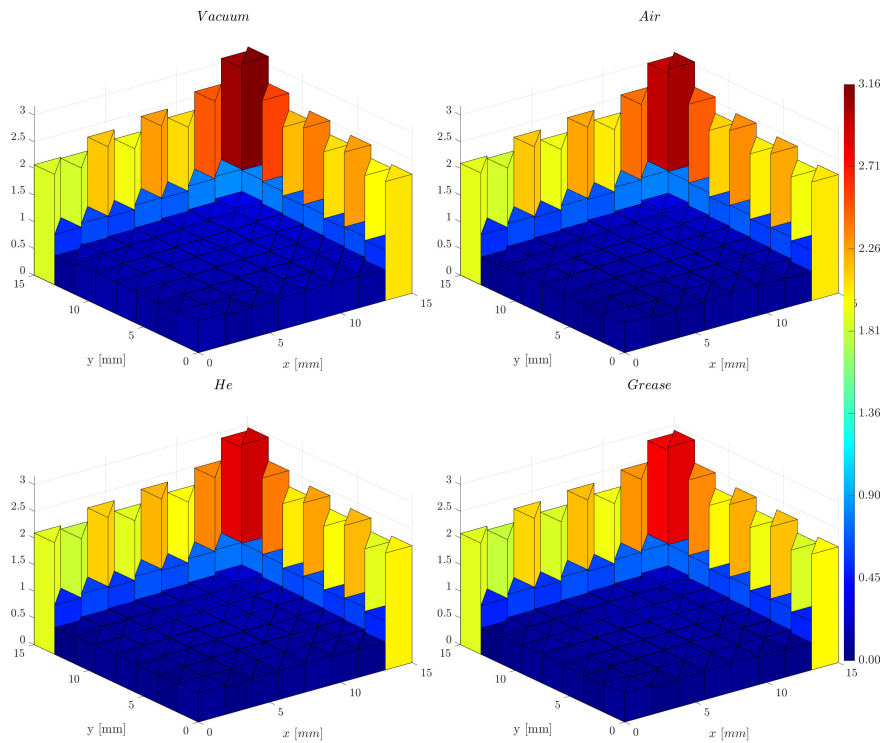


Figure A5. Complete normal traction distribution (t_{n1} [MPa]) comparison at the potential contact zone for all the TIMs analyzed.

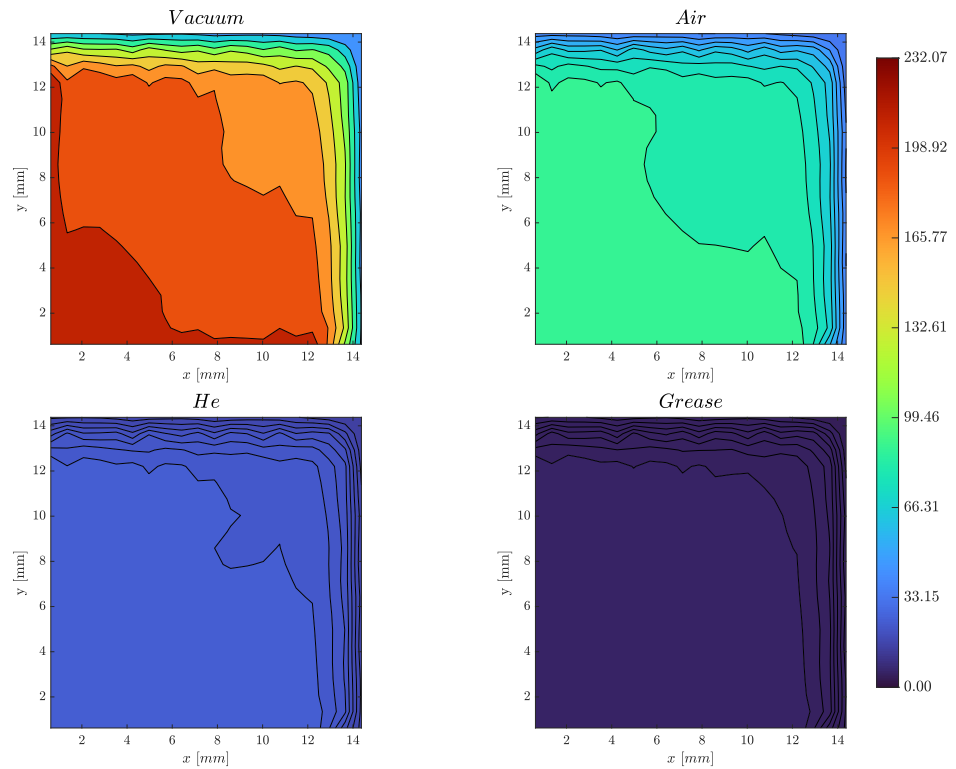


Figure A6. Complete thermal contact resistance (R_{TC} [°Cmm²/W]) comparison at the potential contact zone.

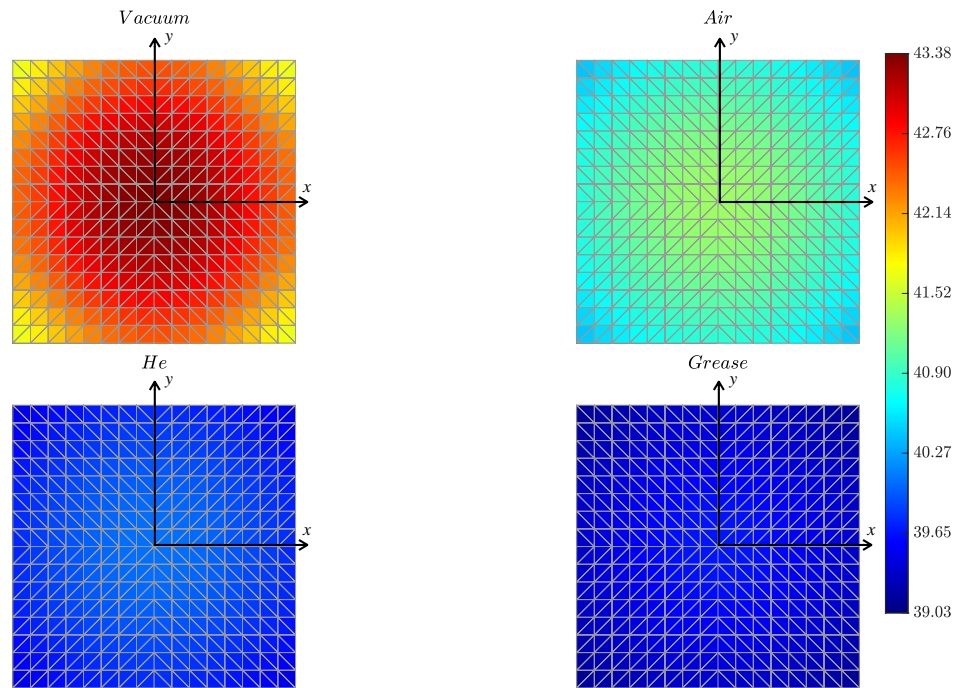


Figure A7. Complete temperature distribution θ [°C] comparison on the base of the microprocessor for each TIM analyzed.

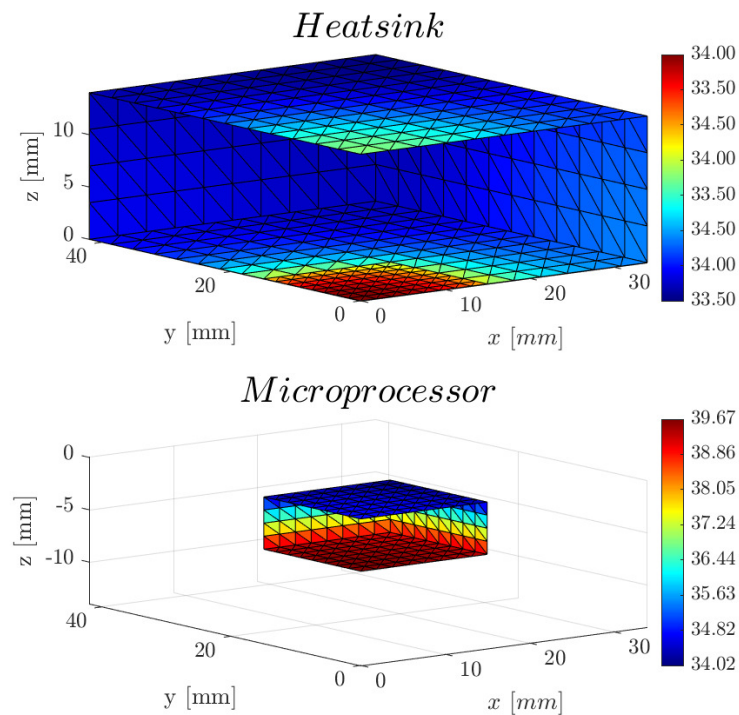


Figure A8. Temperature distribution θ [°C] of the boundary of the microprocessor and the heatsink when a thermal grease fills the interface microgaps.

Appendix A.3. Case of Study 3

In this section, additional figures are included for case study 3. The maximum temperature distribution in the contact zone is shown.

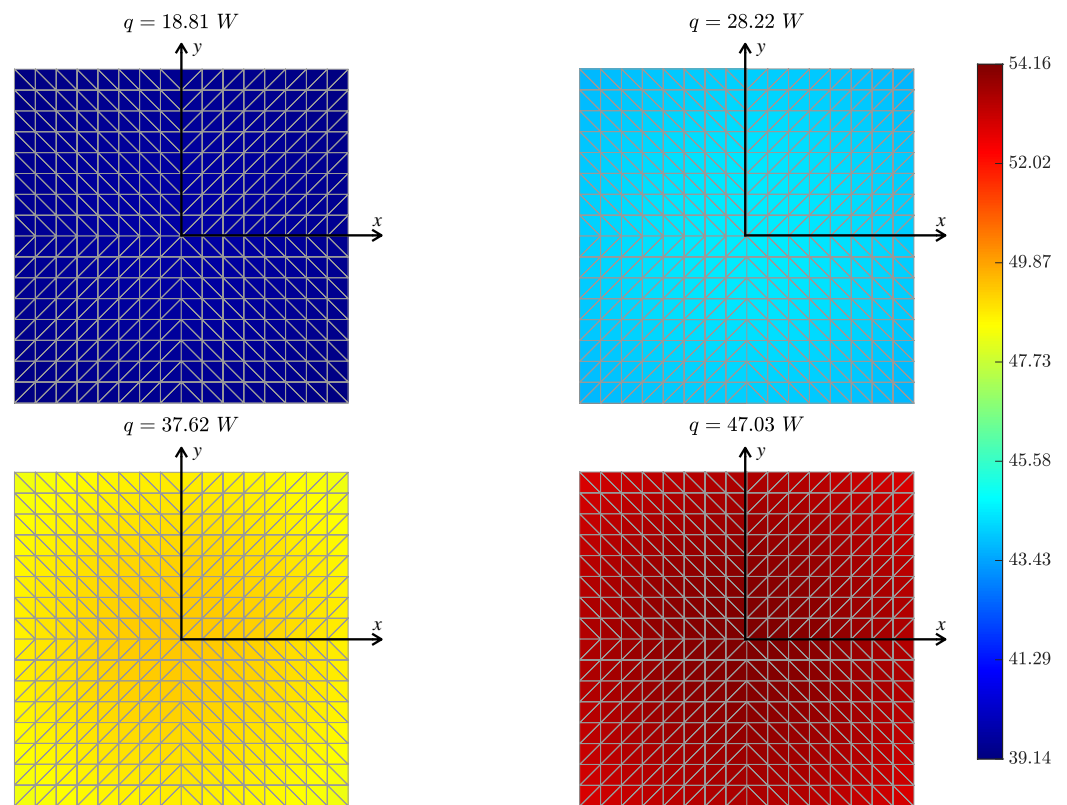


Figure A9. Maximum temperature at the base of the microprocessor for: $q = 18.81\text{ W}$, $q = 28.22\text{ W}$, $q = 37.62\text{ W}$ and $q = 47.03\text{ W}$.

References

- Vallepuga-Espinosa, J.; Ubero-Martinez, I.; Rodríguez-Tembleque, L.; Cifuentes-Rodríguez, J. A boundary element procedure to analyze the thermomechanical contact problem in 3D microelectronic packaging. *Eng. Anal. Bound. Elem.* **2020**, *115*, 28–39. [[CrossRef](#)]
- Vallepuga-Espinosa, J.; Sánchez-González, L.; Ubero-Martínez, I. Winkler Support Model and Nonlinear Boundary Conditions Applied to 3D Elastic Contact Problem Using the Boundary Element Method. *Acta Mech. Solida Sin.* **2019**, *32*, 230–248. [[CrossRef](#)]
- Cooper, M.G.; Mikic, B.B.; Yovanovich, M.M. Thermal contact conductance. *Int. J. Heat Mass Transf.* **1968**, *12*, 279–300. [[CrossRef](#)]
- Savija, I.; Yovanovich, M.M.; Culham, J.R. Thermal joint resistance of conforming rough surfaces with grease-filled interstitial gaps. *J. Thermophys. Heat Transf.* **2003**, *17*, 278–282. [[CrossRef](#)]
- Bahrami, M.; Culham, J.R.; Yovanovich, M.M. Modelling thermal contact resistance: A scale analysis approach. *J. Heat Transf.* **2003**, *126*, 37–44.
- Ubero-Martinez, I.; Rodríguez-Tembleque, L.; Cifuentes-Rodríguez, J.; Vallepuga-Espinosa, J. Non-linear interface thermal conditions in three-dimensional thermoelastic contact problems. *Comput. Struct.* **2020**, *241*, 106354. [[CrossRef](#)]
- Vermeersch, B.; Mey, G.D. BEM calculation of the complex thermal impedance of microelectronic devices. *Eng. Anal. Bound. Elem.* **2007**, *31*, 289–298. [[CrossRef](#)]
- Vermeersch, B.; Mey, G.D. Influence of thermal contact resistance on thermal impedance of microelectronic structures. *Microelectron. Reliab.* **2007**, *47*, 1233–1238. [[CrossRef](#)]
- Jang, S.P.; Choi, S.U.S. Cooling performance of a microchannel heat sink with nanofluids. *Appl. Therm. Eng.* **2006**, *26*, 2457–2463. [[CrossRef](#)]
- Zhang, H.Y.; Mui, Y.C.; Tarin, M. Analysis of thermoelectric cooler performance for high power electronic packages. *Appl. Therm. Eng.* **2010**, *30*, 561–568. [[CrossRef](#)]
- Mey, G.D.; Pilarski, J.; Wójcik, M.; Lasota, M.; Banaszcyk, J.; Vermeersch, B.; Napieralski, A. Influence of interface materials on the thermal impedance of electronic packages. *Int. Commun. Heat Mass Transf.* **2009**, *36*, 210–212. [[CrossRef](#)]
- Ha, M.; Graham, S. Development of a thermal resistance model for chip-on-board packaging of high power LED arrays. *Microelectron. Reliab.* **2012**, *52*, 836–844. [[CrossRef](#)]
- Zavarise, G.; Wriggers, P.; Stein, E.; Schrefler, B.A. Real contact mechanisms and finite element formulation. A coupled thermomechanical approach. *Int. J. Numer. Methods Eng.* **1992**, *35*, 767–785. [[CrossRef](#)]
- Wriggers, P.; Zavarise, G. Thermomechanical contact—A rigorous but simple numerical approach. *Comput. Struct.* **1993**, *46*, 47–53. [[CrossRef](#)]

15. Johansson, L.; Klarbring, A. Thermoelastic frictional contact problems: Modelling, finite element approximation and numerical realization. *Comput. Methods Appl. Mech. Eng.* **1993**, *105*, 181–210. [[CrossRef](#)]
16. Strömberg, N. Finite Element treatment of two-dimensional thermoelastic wear problems. *Comput. Methods Appl. Mech. Eng.* **1999**, *177*, 441–455. [[CrossRef](#)]
17. Ireman, P.; Klarbring, A.; Strömberg, N. Finite element algorithms for thermoelastic wear problems. *Eur. J. Mech. A/Solids* **2002**, *21*, 423–440. [[CrossRef](#)]
18. Strömberg, N. An Eulerian approach for simulating frictional heating in disc-pad systems. *Eur. J. Mech. A/Solids* **2011**, *30*, 673–683. [[CrossRef](#)]
19. Patunso, D.; Klaus-Jürgen Bathe, P.A.B. A finite element procedure for the analysis of thermomechanical solids in contact. *Comput. Struct.* **2000**, *75*, 551–573.
20. Hüeber, S.; Wohlmuth, B.I. Thermo-mechanical contact problems on non-matching meshes. *Comput. Methods Appl. Mech. Eng.* **2009**, *198*, 1338–1350. [[CrossRef](#)]
21. Seitz, A.; Wall, W.A.; Popp, A. Nitsche's method for finite deformation thermomechanical contact problems. *Comput. Mech.* **2019**, *63*, 1091–1110. [[CrossRef](#)]
22. Aliabadi, F.M.H. *The Boundary Element Method: Applications in Solids and Structures*; Wiley: Chichester, UK, 2002; Volume 2.
23. Alonso, P.; Garrido García, J. BEM applied to 2D thermoelastic contact problems including conduction and forced convection in interstitial zones. *Eng. Anal. Bound. Elem.* **1995**, *15*, 249–259. [[CrossRef](#)]
24. Giannopoulos, G.I.; Anifantis, N.K. A BEM analysis for thermomechanical closure of interfacial cracks incorporating friction and thermal resistance. *Comput. Methods Appl. Mech. Eng.* **2007**, *196*, 1018–1029. [[CrossRef](#)]
25. Vallepuga Espinosa, J.; Foces Mediavilla, A. Boundary element method applied to three dimensional thermoelastic contact. *Eng. Anal. Bound. Elem.* **2012**, *36*, 928–933. [[CrossRef](#)]
26. Vallepuga-Espinosa, J.; Ubero-Martínez, I.; Sánchez, L.; Cifuentes-Rodríguez, J. An incremental-iterative BEM methodology to solve 3D thermoelastic contact problem including variable thermal resistance in the contact zone. *Contin. Mech. Thermodyn.* **2019**, *31*, 1543–1558. [[CrossRef](#)]
27. Ubero-Martínez, I.; Vallepuga-Espinosa, J.; Rodríguez-Tembleque, L.; Cifuentes-Rodríguez, J. The effect of conduction and convective conditions at interstitial regions on 3D thermoelastic contact problems. *Eng. Anal. Bound. Elem.* **2019**, *107*, 243–256. [[CrossRef](#)]
28. Vallepuga-Espinosa, J.; Ubero-Martínez, I.; Cifuentes-Rodríguez, J.; Rodríguez-Tembleque, L. Thermoelastic influence of convective and conduction interstitial conditions on the size of the contact zone in three-dimensional receding thermoelastic contact problem. *Acta Mech.* **2020**, *231*, 3065–3084. [[CrossRef](#)]
29. Ubero-Martínez, I.; Rodríguez-Tembleque, L.; Cifuentes-Rodríguez, J.; Vallepuga-Espinosa, J. 3D thermoelastic solids under non-linear interface thermal and orthotropic frictional contact conditions. *Int. J. Numer. Methods Eng.* **2022**, *123*, 2631–2659. [[CrossRef](#)]
30. Rodríguez-Tembleque, L.; Abascal, R. Fast FE-BEM algorithms for orthotropic frictional contact. *Int. J. Numer. Methods Eng.* **2013**, *94*, 687–707. [[CrossRef](#)]
31. Rodríguez-Tembleque, L.; Buroni, F.C.; Abascal, R.; Sáez, A. Analysis of FRP composites under frictional contact conditions. *Int. J. Solids Struct.* **2013**, *50*, 3947–3959. [[CrossRef](#)]
32. Rodríguez-Tembleque, L.; Aliabadi, M.H. Numerical simulation of fretting wear in fiber-reinforced composite materials. *Eng. Fract. Mech.* **2016**, *168*, 13–27. [[CrossRef](#)]
33. Rodríguez-Tembleque, L.; García-Macías, E.; Sáez, A. CNT-polymer nanocomposites under frictional contact conditions. *Compos. Part B Eng.* **2018**, *154*, 114–127. [[CrossRef](#)]
34. Greenwood, J.A.; Williamson, J.P. Contact of nominally flat surfaces. *Proc. R. Soc. Lond.* **1966**, *295*, 300–319.
35. Savija, I.; Culham, J.; Yovanovich, M.M. Effective thermophysical properties of thermal interface materials: Part I: Definitions and models. In Proceedings of the International Electronic Packaging Technical Conference and Exhibition, Maui, HI, USA, 6–11 July 2003.
36. Yovanovich, M.M.; Culham, J.R.; Teertstra, P. Calculating Interface Resistance. *Electron. Cool.* **1997**, *3*, 1–9.
37. Song, S.; Yovanovich, M.M. Explicit Relative Contact Pressure Expression: Dependence upon roughness parameters and vickers microhardness coefficients. In Proceedings of the 25th AIAA Aerospace Sciences Meeting, Reno, NV, USA, 24–26 March 1987.
38. Yovanovich, M.M. Micro and Macro Hardness Measurements, Correlations, and Contact Models. In Proceedings of the 44th AIAA Aerospace Sciences Meeting and Exhibit, Reno, NV, USA, 9–12 January 2006.
39. Zavarise, G.; Wriggers, P.; Stein, E.; Schrefler, B.A. A numerical model for thermomechanical contact based on microscopic interface laws. *Mech. Res. Commun.* **1992**, *19*, 173–182. [[CrossRef](#)]
40. Alonso, P. Thermoelastic Contact Problem Using BEM. Ph.D. Thesis, Universidad de Valladolid, Valladolid, Spain, 1995.
41. Foces Mediavilla, A. Tridimensional Elastic Contact Problem by Boundary Integrals. Ph.D. Thesis, University of Valladolid, Valladolid, Spain, 1991.
42. París, F.; Foces, A.; Garrido, J. Application of boundary element method to solve three-dimensional elastic contact problems without friction. *Comput. Struct.* **1992**, *43*, 19–30. [[CrossRef](#)]